LBL-17914

Lawrence Berkeley Laboratory

UNIVERSITY OF CALIFORNIA

RECEIVED
LAWRENCE
BERKELEY LABORATORY

NOV 20 1984

LIBRARY AND
DOCUMENTS SECTION

Materials & Molecular Research Division

Presented at The Physics of Chaos and Related Problems (Nobel Symposium), Gräftavallen, Sweden, June 11-16, 1984; and to be published in Physica Scripta

CHAOTIC DYNAMICS OF INSTABILITIES IN SOLIDS

C.D. Jeffries

May 1984

TWO-WEEK LOAN COPY

This is a Library Circulating Copy which may be borrowed for two weeks.

Prepared for the U.S. Department of Energy under Contract DE-AC03-76SF00098

LBL-17914

DISCLAIMER

This document was prepared as an account of work sponsored by the United States Government. While this document is believed to contain correct information, neither the United States Government nor any agency thereof, nor the Regents of the University of California, nor any of their employees, makes any warranty, express or implied, or assumes any legal responsibility for the accuracy, completeness, or usefulness of any information, apparatus, product, or process disclosed, or represents that its use would not infringe privately owned rights. Reference herein to any specific commercial product, process, or service by its trade name, trademark, manufacturer, or otherwise, does not necessarily constitute or imply its endorsement, recommendation, or favoring by the United States Government or any agency thereof, or the Regents of the University of California. The views and opinions of authors expressed herein do not necessarily state or reflect those of the United States Government or any agency thereof or the Regents of the University of California.

LBL-17914

To be published in Physica Scripta.

CHAOTIC DYNAMICS OF INSTABILITIES IN SOLIDS*

Carson D. Jeffries

Physics Department, Univ. of California, Berkeley, CA 94720

and

MMRD, Lawrence Berkeley Laboratory, Berkeley, CA 94720

May 1984

*This work was supported by the Director, Office of Energy Research, Office of Basic Energy Sciences, Materials Sciences Division of the U.S. Department of Energy under Contract No. DE-AC03-76SF00098.

To be published in Physica Scripta,
Proceedings of Nobel Symposium on
The Physics of Chaos and Related Problems,
Gräftavallen, Sweden, June 11-16, 1984

CHAOTIC DYNAMICS OF INSTABILITIES IN SOLIDS

Carson D. Jeffries

Physics Department, Univ. of California, Berkeley, CA 94720 USA

and

MMRD, Lawrence Berkeley Laboratory, Berkeley, CA 94720 USA

Abstract

A review is given of studies of chaotic dynamics in several solid state systems. In each case the physical system is described, relevant equations of motion are given, experimental results are presented and interpreted, more or less, from the relevant equations, including numerical solutions. The systems are: (1) An electron-hole helical plasma density wave in a Ge crystal in parallel electric and magnetic fields; this shows period doubling and quasiperiodic routes to chaos. (2) Standing mode spin wave packets in ferrite spheres, excited by driving ferromagnetic resonance of the uniform mode; this system shows period doubling to chaos and periodic windows. (3) Resonantly driven p-n junctions in Si show extremely nonlinear behavior due to charge stored during injection; one junction shows period doubling to chaos and period adding (frequency locking); coupled junctions show, in addition, quasi-periodicity, entrainment, and behavior generic to coupled nonlinear oscillators. The fractal dimension is measured for these systems.

Physics Abstracts Classification: Instabilities in plasmas (5235); Fluid turbulence (4725J&M); Spin waves (7530D); Statistical mechanics and fluctuations (0540).

TABLE OF CONTENTS

0. Abstract

1. Introduction

2. p-n junctions in silicon

   2.1 Physical system and models

   2.2 A driven p-n junction: results and interpretation

   2.3 Systems of coupled p-n junction resonators

   2.4 N=2 coupled resonators: results and interpretation

3. Electron-hole plasmas in germanium crystals

   3.1 Plasma system and models

   3.2 Experimental results and interpretation

4. Spin waves in ferrite spheres

   4.1 Spin system and models

   4.2 Experimental results and interpretation

5. Summary and conclusions

Acknowledgments

References

Figure Captions

Figures

1. INTRODUCTION

Over the years experimental solid state physicists have discovered a number of dynamical instabilities in many physical systems, e.g. semiconductors and magnetic substances, characterized often by onset of oscillations, hysteresis, and erratic behavior when suitably excited. In many cases theoretical analyses have been given. Their microscopic origins can be ascribed to nonlinear coupling between model elementary excitations, e.g., phonons, plasmons, magnons, holes, excitons, etc., and external driving fields. Earlier workers did not have the advantage of the present theoretical framework, especially the ideas of universality [1] and recognizable routes to chaos [2]; the data were not taken in a format that could easily reveal such behavior. Just as in fluids, experimental studies of instabilities in solids are of renewed interest.

I will review recent Berkeley work on instabilities in three systems: p-n junctions in Si; electron-hole plasmas in Ge crystals; and spin waves in ferrite spheres. For each case I describe the physical system, indicate the equations of motion and the source of nonlinearity, and the experimental results and their interpretation.

2. P-N JUNCTIONS IN SILICON

A p-n junction when resonantly driven will exhibit a period doulbing cascade to chaos [3]. Related instabilities were observed in early work on parametric amplifiers using diodes but were not so well understood [4]. Driven junctions have been used for the study of intermittency [5], effects of added noise [6,7], crises of the attractor [8,9], and the quasiperiodic route to chaos when two or more are coupled together [10,11]. The system is approximately

modeled by a driven asymmetric passive oscillator (i.e., a resonator) with a very nonlinear restoring force, but the model is not exact. The system is clearly not an analog computer

2.1 Physical system and models. The junction, Fig. 1, is composed of a Si crystal containing fixed donor ions (+) and electrons (•) to the right and fixed acceptor ions (-) and holes (o) to the left of a doping interface in a region $\sim 10^{-4}$ cm wide. One solves the transport equation, including drift and mobility terms in an electric field arising from an applied potential difference V [12]. One finds for V negative that the junction is approximated by a junction differential capacitance $C_j(V) = C_{jo}[1-V/\Phi]^{-\frac{1}{2}}$; this arises from the fixed (+) and (-) ions in the interface. For V positive, holes (electron) are injected into the n(p) regions and give rise to a large storage differential capacitance $C_s(V) = C_{so}\exp(V/\phi)$ and a junction current $I_d(V) = I_o[\exp(V/\phi) - 1]$ for an ideal diode. The injected carriers recombine or back-diffuse in a characteristic minority carrier lifetime τ. If the junction is resonantly driven by a voltage $V_o = V_{os}\sin\omega t$ with $(2\pi/\omega) \gtrsim \tau$, then the equations of motion of the system, Fig. 1, become

C_{jo}, Φ, C_{so}, ψ, and I_o are measurable parameters for a given junction.

$$\dot{I} = \frac{V_o(\theta) - RI - V}{L} \tag{1a}$$

$$\dot{V} = \frac{I - I_d(V)}{C(V)} \tag{1b}$$

$$\dot{\theta} = \omega \tag{1c}$$

where $\theta = \omega t$ and $C(V) = C_j(V) + C_s(V) = (\partial Q/\partial V)$ is the total differential capacitance. The motion can be visualized in I, V, θ

polar coordinates chosen so that the orbits traverse the I, V plane at, say, $\sin\Theta = 0$ at consecutive times $t = nT$. This Poincaré section of the attractor can be observed directly by displaying I, V on an oscilloscope and strobing the beam intensity at $t = nT$. Alternatively, one displays $(\dot{I}, I)$ or (I_{n+1}, I_n), which are conjectured to be topologically equivalent [13]. Equations (1) are stiff, display a slow and a fast manifold [14], and can be numerically integrated by an explicit fourth order Runge-Kutta algorithm [15].

Equations (1) are of the form

$$dx_i(t)/dt = f_i[x_1(t), x_2(t), x_3(t)]_{i=1,2,3} \tag{2}$$

discussed by Ott [16], and have a negative divergence of phase space flow $\Sigma_i \partial f_i/\partial x_i$, approximately equal to the value $-|a|$ in Eq. (3); volumes in phase space decrease exponentially in time, $\Lambda(t) = \Lambda(o)\exp(-at)$. Since the system is observed to display chaotic motion one can thus conclude that it has a strange attractor characterized by a fractal dimension. Some physical insight is obtained by calculating the effective charge on the junction

$$q(V) = \int_0^V C(V)dV,$$

and rewriting Eqs. (1) in the form of a driven damped nonlinear oscillator

$$\ddot{q} + a(q)\dot{q} - f(q) = A_o \sin\omega t, \tag{3}$$

with a damping coefficient

$$a(q) = \frac{R}{L} + \frac{1}{C(q)}\frac{\partial I_d}{\partial V} \tag{4a}$$

and a restoring force

$$f(q) = -\frac{1}{L}[V(q) + RI_d(V(q))] . \tag{4b}$$

This force function for typical system parameters shows a weak, almost constant form for positive q (forward injection) and a strong exponentially increasing force for negative q. The expansion of Eq. (4), $f(q) \approx -Aq + Bq^2 - Cq^3 + Dq^4 \ldots$, shows no symmetry so that the system may display period doubling without first undergoing symmetry breaking [17], in contrast to the driven pendulum and Duffing's equation, $f(q) \sim -q \pm q^3$. For large q, the force can be roughly modeled by the form $f(q) \approx \exp(-q) - 1$; and by $f(q) \approx -\log(q+1)$ if one assumes $C_j \ll C_s$, a reasonable approximation for some junctions. In this case the junction oscillator is so nonlinear that it can be experimentally driven hard enough to shift its resonance frequency down by an order of magnitude - an ultra-soft spring.

If Eqs. (1) or (3) are numerically solved, the computed Poincaré section and the return map are found to be essentially one-dimensional if the dissipation a(q) in Eq. (3) is large enough. More generally, however, they are described by a two-dimensional map of the form

$$x_{n+1} = f(x_n, y_n, A) \tag{5a}$$

$$y_{n+1} = g(x_n, y_n, A) \tag{5b}$$

where A is the set of system parameters. From the physical fact that the minority carrier density recovery after forward injection is a diffusion time processes, the motion is more properly described by differential delay equations rather than the approximation, Eqs. (1) and (3). In *principle* the system is very high-dimensional and Eqs. (5) should perhaps be modified to $x_{n+1} = f(x_n, x_{n-1}, x_{n-2}, \ldots y_n, y_{n-1}, \ldots, A)$, although present data do

not seem to require this, owing to the dissipation. The question can be rephrased: how many previous cycles can the system remember?

2.2 A driven p-n junction: experimental results and interpretation. We measure the set $\{I_n\}$ of consecutive current maxima by a sampling $I(t)$, and plot this set vs. the magnitude V_{os} of the drive voltage, thus obtaining a bifurcation diagram, e.g. that shown in Fig. 2. In general, observed bifurcation diagrams may deviate very considerably from Fig. 2 and depend markedly on the system parameters ω, R, L, C_{jo}, C_{so}, I_o, Φ, and ϕ contained in Eqs. (1) and in (3), as well as the carrier lifetime τ. This is an experimental manifestation of the sensitivity of instabilities to system parameters in a complex system. However, diagrams like Fig. 2 are observed if the parameters are so chosen that: (i) the drive frequency $\omega \simeq \omega_{res} \simeq [L(C_{so} + C_{jo})]^{-\frac{1}{2}}$ = resonance frequency of the junction oscillator at $V_{os} \sim 0$; (ii) $(2\pi/\omega) \sim \tau$, within a factor 10; (iii) the damping coefficient $a(q)$ in Eq. (3) is large enough; (iv) V_{os} is not too large. Under these conditions almost all p-n junctions studied (approximately 10 different types) display a bifurcation diagram like Fig. 2, which is the *simplest* type observed, with recognizable universal features.

There is clearly a cascade of period doubling bifurcations to an accumulation point of chaos, band merging, periodic windows, and the onset of a wide period 3 window with hysteresis. Very roughly the behavior follows a special simple case of Eqs. (5),

$$x_{n+1} = 1 - Ax_n^2 , \tag{6}$$

the logistic map [18] with the correspondence $I \rightarrow x$ and $V_{os} \rightarrow A$, the control parameter. The Poincaré section of the numerical solution of Eq. (3) with $a(q) \simeq a \gtrsim 1$ is essentially one-dimensional and can be parameterized by a unimodal return map [11].

Figure 3 shows the measured power spectrum of the voltage V across a driven p-n junction for a set of increased values of V_{os}, showing period doubling, chaos (four-band), chaos (one-band).

Another characteristic bifurcation diagram displayed by all junctions if they can be driven hard enough and a(q) is not too large, is shown in Fig. 4(a), together with a plot of the junction current $\overline{I(t)} = \overline{I}$, average over one cycle. In addition to period doubling to chaos, there is a sequence of periodic regions, of periods 3, 4, 5, ...N, ... which we refer to as period adding. This has a simple physical explanation. It is seen that $\overline{I}$ is approximately constant in a region of period N, and furthermore we observe $N^{-1} \propto (\overline{I})^{-\frac{1}{2}}$. For hard driving, the dominant junction capacitance is $C_s \propto \exp(V/\phi)$, which is just proportional to the junction current I_d for large forward injection. Thus the resonant frequency of the junction oscillator $\omega_{res} \propto (C_s)^{-\frac{1}{2}} \propto (\overline{I})^{-\frac{1}{2}}$, which is just the frequency ω/N of a periodic region. That is, as this soft spring system is driven harder, it shifts its frequency down and becomes entrained or locked at successive subharmonics of the drive frequency; it is a passive nonlinear resonator with entrainment behavior resembling a driven van der Pol self-oscillator. Figure 5 is a two-parameter diagram of the observed entrainment regions.

Figure 6 shows the observed projection of the attractor in the $(\dot{I}, I)$ plane at a drive voltage for which the $2 \rightarrow 1$ band merge has occurred. The faint oval lines correspond to the veils in the bifurcation diagram, Fig. 3, and are successive iterates of the critical point of the map. The dark line is a Poincaré section made

by enhancing the oscilloscope intensity at $\theta(t) = 0$. This section is not really one-dimensional. The observed return map (I_n, I_{n+1}, I_{n+2}) of Fig. 7(b) clearly shows this, and can be reasonably fit by the two-dimensional Hénon map [19],

$$x_{n+1} = 1 + Bx_{n-1} - Ax_n^2 \tag{7}$$

with $A = 1.5$ and $B = 0.08$, shown in Fig. 7(a). This value of B, the phase volume contraction per cycle, is typical for junction oscillators with moderate driving. Equation (7) can explain the observed hysteresis, which Eq. (6) cannot. However, Eq. (7) cannot fit the data for hard driving into the period adding region, Fig. 4, where the return map of Fig. 7(c) is observed, in the chaotic band between periods 4 and 5.

A high resolution Poincaré section for this region, Fig. 8, clearly shows self-similarity [19] and the fractal [20] structure of the attractor. A set of measurements of the fractal dimension d [21] of the attractor for a driven p-n junction has been carried out by Held et al. [22] with the preliminary result for the chaotic region just below the period 3 window, $d = 2.05 \pm 0.05$. This measure is related to

$$d_c \equiv \lim_{\varepsilon \to 0} \frac{\log N(\varepsilon)}{\log(1/\varepsilon)} , \tag{8}$$

a common definition of measure of dimension [21]. Our computation procedure is discussed in Sec. 3.2. This same value of d was observed for two quite different types of p-n junctions.

The results of a two-parameter study [10] of the overall behavior of a driven junction is given in the "phase diagram" of Fig. 9, showing the boundaries of the various periodic and chaotic regions as a function of the driving voltage V_{os} and the driving frequency $f = \omega/2\pi$. The "simplest" bifurcation diagram, e.g. Fig. 2, is obtained by increasing V_{os} upward along a line of constant frequency $\simeq$ 20 kHz $\simeq$ junction oscillator resonance frequency. Moving upward along f = 34 kHz gives a periodic sequence 1, 2, 4, 8, 4, 2, 1 without chaos. Increasing f horizontally at constant voltage V_{os} = 2 volts generates 1, 2, 4, 8, ...chaos, ...8, 4, 2, 1. Figure 9 makes clear why such a wide variety of bifurcation diagrams are observed; even more variation occurs in a three-parameter space, the third parameter being the dissipation coefficient a in Eq. (3). Figure 9 also

indicates hysteresis ($\uparrow,\downarrow$) and a period $1 \rightarrow$ period 1 bifurcation, the "jump phenomena," characteristic of driven nonlinear oscillators [23] and an example of a transcritical bifurcation [24].

The detailed behavior can be fit fairly well by the numerical integration of Eqs. (1) or (3) using the known system parameters. Figure 10 is the computed bifurcation diagram for the charge $\{q\}$ vs. A_0 from solution of Eq. (3), with $a(q) \approx a = 0.45$ and $\omega = 1$. It can be compared to current data $\{I\}$ vs. V_{os}, Fig. 2, showing reasonable correspondence including hysteresis. Bifurcation data showing extensive period adding, Fig. 4, can be fit by maps of the form of Eq. (5) to generate the bifurcation diagram of Fig. 11, which is computed from the map [11]

$$x_{n+1} = [x_n + 1 - S(x_n)] - S(A(1 - S(x_n)^2)) - y_n \tag{9a}$$

$$y_{n+1} = Bx_n \tag{9b}$$

$$S(x) = \tfrac{1}{2}(x + \sqrt{x^2 + B}) \tag{9c}$$

with $B = 0.1$ and A the control parameter. These equations generate return maps similar to observations, Fig. 7(c).

By applying a short perturbing pulse to the driven junction, one can measure the transient recovery time τ_c of the junction current to its steady state value as a function of the drive voltage V_{so} near the $1 \rightarrow 2$ bifurcation point V_{cr}. This plot, Fig. 12, displays the critical-slowing-down phenomena characteristic of phase transitions. Other experimental evidence of universal behavior of driven junctions is given by comparison of theoretical prediction for scaling with measured values for: period doubling convergence rate δ [3];

pitchfork ratio α [3]; power spectral ratio [3]; noise sensitivity factor κ [6]; noise scaling at bifurcation points [7]; and intermittency route scaling [5]. To summarize, the driven junction is well characterized and appropriate to use in systems composed of large numbers coupled together.

2.3 Systems of coupled p-n junction resonators [10,11]. It is experimentally straightforward to couple together N identical p-n junction resonators and force the system by a common driving oscillator. This can be done in many ways, but we discuss only these two, with different symmetry: (i) resistive coupling: connect a second inductance plus junction between A and C in Fig. 1; (ii) inductive coupling: connect second inductance plus junction between B and C with $R \approx 0$. The approximate equations of motion, following Sec. 2.1 and Eqs. (3) and (4) take the form

$$\ddot{q}_1 + \beta[a\dot{q}_1 + r(\dot{q}_1 + \dot{q}_2)] - f(q_1) = A_0 \sin\omega t \tag{10a}$$

$$\ddot{q}_2 + a\dot{q}_2 + r(\dot{q}_1 + \dot{q}_2) - f(q_2) = A_0 \sin\omega t \tag{10b}$$

for resistive coupling where r is the coupling parameter, a is the dissipative coefficient, and $\beta \lesssim 1$ is a factor to account for the fact that the p-n junctions, in practice, are not identical. For the inductive coupling case,

$$\ddot{q}_1 + a\dot{q}_1 - 2f(q_1) + f(q_2) = A_0 \sin t \tag{11a}$$

$$\ddot{q}_2 + a\dot{q}_2 - f(q_2) + f(q_1) = 0 \tag{11b}$$

In contrast to a simple driven resonator, for $N \geq 2$ coupled resonators we expect Hopf bifurcations to quasiperiodicity, in

addition to period doubling bifurcations and intermittency; Eqs. (10) and (11) do exhibit this behavior. One expects quite generally that their Poincaré sections will be described by two coupled maps of the plane

$$x_{n+1} = f(x_n, y_n, X_n, Y_n, \Lambda) \tag{12a}$$

$$y_{n+1} = g(x_n, y_n, X_n, Y_n, \Lambda) \tag{12b}$$

$$X_{n+1} = h(x_n, y_n, X_n, Y_n, \Lambda) \tag{12c}$$

$$Y_{n+1} = l(x_n, y_n, X_n, Y_n, \Lambda) \tag{12d}$$

and that these will reduce to simpler forms with sufficient dissipation. A related map, a circle map modeling a single forced self-excited oscillator, has received recent attention in computation of universal features of the quasiperiodic route to chaos [25].

2.4 <u>N=2 coupled oscillators: results and interpretation [10,11]</u>. Figure 13 shows a bifurcation diagram observed for the resistively coupled case driven at frequency f_1 and amplitude V_{os}. It is characterized by period doubling to $f_1/2$ and then a Hopf bifurcation to a second incommensurate frequency f_2; narrow regions of entrainment or locking with f_2/f_1 a rational number M/N [see blow-up in Fig. 13(b)]; a wide locking region with relative period 18; period doubling to 36, ... to two-band chaos; and abrupt change of attractor (a crisis [8]); etc. This figure shows the clear distinction in a bifurcation diagram between period doubling and Hopf bifurcations.

The results of a two-parameter study of the overall behavior in the quasiperiodic region are shown in the phase diagram, Fig. 14,

to be compared to Fig. 9, for a single junction. Along the boundary line of the Hopf bifurcation the frequency ratio f_2/f_1 varies continuously from 0.211319... (upper left) to 0.23018... (upper right), and when $f_2/f_1 \rightarrow M/N$, a point of resonance, there emanates from the boundary a horn-shaped entrainment domain similar to that observed for Hopf bifurcations in a detailed study of a driven magnetic oscillator [26], and corresponding to the resonance horns predicted by Arnold [27]. The horns are labeled in Fig. 14 by the integer N/2 which is just the number of fixed points in the upper branch of the Poincare section, e.g., Fig. 16(d). The integer M is then determined from the strongest line f_2 in the measured power spectrum, e.g., Fig. 18(b). There are many other narrow entrainment horns, not shown. Period doubling to chaos occurs within an entrainment horn. When horns overlap, there is intermittency and hysteresis between two attractors. The regions of chaos are widespread and fall approximately within the heavy dashed parabolic region of Fig. 14. We have some evidence that the upper Hopf bifurcation boundary becomes closed for drive voltages much larger than shown.

For an inductively coupled system, Fig. 15 shows a sequence of phase portrait projections in the $(\dot{I}, I)$ plane for increasing drive, along with a darker strobed Poincaré section at $\theta(t) = 0$. For this system there is first a Hopf bifurcation in contrast to the resistively coupled case. The period 1 orbit in Fig. 15(a) becomes a 2-torus in 15(b), with Poincaré section becoming rather square as the quasiperiodic orbit becomes periodic with M/N = 1/4 just beyond Fig. 15(d).

Figures 16 and 17 show a sequence of eight Poincaré sections (V_1, I_2) for resistive coupling, showing the characteristic breakup of the invariant circle with increasing drive voltage, corresponding to moving vertically upward on Fig. 14 along a line of constant frequency $\simeq$ 29.5 kHz. Figures 18(a)-(g) show the power spectra for this exact same sequence. There is first a period doubling, then onset of a Hopf bifurcation with new incommensurate frequency f_2, Fig. 18(a), and combination frequencies $f_1/2 - f_2$ and $f_1/2 + f_2$ (not shown). Figure 18(b) shows combination frequencies $f_{nm} = nf_1/2 + mf_2$ with m, n positive and negative integers. At Figs. 18(d) and 16(d), locking occurs at $f_2/f_1 = 4/18$, and period doubling to 4/36 at Figs. 18(d) and 17(a). Chaos begins in the Poincaré section of Fig. 17(b) in the form of a rabbit(!) whose ears and legs fold over; in Figs. 17(d) and 18(h) there is a two-band chaotic attractor resembling a folded rug.

Figure 19 is another sequence of Poincaré sections (V_1, I_2) for reduced resistive coupling, showing fast oscillations of a rather square orbit as it approaches locking at $f_2/f_1 = 1/4$ to two attractors in the corners. It is less strongly pulled to two other attractors in the other corners; these attractors have a different basin which are accessible by decreasing V_{os} from a large value.

To compare the above results to models, we point out immediately that Fig. 19(d) is strikingly similar to a Poincaré section (x, X) computed by Hogg and Huberman [28] from a special case of Eq. (12), two coupled one-dimensional maps

$$x_{n+1} = rx_n(1 - x_n) + \varepsilon X_n \tag{13a}$$

$$X_{n+1} = rX_n(1 - X_n) + \varepsilon x_n \tag{13b}$$

with $r = 3.39$, $\varepsilon = 0.06$, $x_0 = 0.2$, $X_0 = 0.4$. This shows that the dissipation in the system used is sufficient to approximately reduce the Poincaré space from 4 to 2 dimensions. On the whole, the Poincaré sections observed are similar to those computed from dissipative maps of the plane by a number of authors [29].

Figure 20 is a bifurcation diagram numerically computed from the differential equations [Eqs. (10)]; it shows the principal features of the data, Fig. 13(a). Perhaps better agreement is that shown in Fig. 21 computed from this map constructed to model the p-n junction behavior [11]:

$$x_{n+1} = 0.5[x_n + 1 - S(x_n)] - S(A(1 - S(x_n)^2)) - y_n + CX_n \tag{14a}$$

$$y_{n+1} = 0.1\ x_n \tag{14b}$$

$$X_{n+1} = 0.5[X_n + 1 - S(X_n)] - S(Ab(1 - S(X_n)^2)) - Y_n + Cx_n \tag{14c}$$

$$Y_{n+1} = 0.1\ X_n \tag{14d}$$

$$S(x) = 0.5\ (x + \sqrt{x^2 + 0.1})\ , \tag{14e}$$

with C = coupling parameter = 0.3, b = asymmetry parameter = 0.95, A = control (drive) parameter.

A two-parameter plot in ω and A_0 of computed solutions of Eqs. (10) will moderately fit the shape of the Hopf boundary in Fig. 14 and also the boundary of the $1 \rightarrow 2$ period doubling bifurcation (not shown in Fig. 14 but similar to that in Fig. 9).

Similar experiments for N=2 for the inductively coupled case show that a Hopf bifurcation occurs first -- and this is in agreement with the models of Eqs. (11) and also of maps similar to Eqs. (14) but with the *sign* of the coupling term reversed in Eq. (14c); this is a direct consequence of a different symmetry. For N=12 coupled junctions, Hopf bifurcations to three incommensurate frequencies are observed [11].

The attractor dimension d has been measured [22] for the system shown in Fig. 17(d), with the preliminary values $d = 2.23 \pm 0.05$, to be compared to 2.05 ± 0.05 for a single driven junction.

3. ELECTRON-HOLE PLASMAS IN GERMANIUM CRYSTALS

Plasmas in semiconductors have been extensively studied experimentally and show a number of instabilities [30]. However, chaotic dynamics has only been observed recently by Held et al. [31] in experiments on plasma density waves in crystals of Ge. Chaotic dynamics due to impact ionization and space charge injection in Ge has been reported by Teitsworth, Westervelt, and Haller [32]. The system we study is spatially continuous with very many degrees of freedom and is modeled by a set of partial differential equations. It exhibits both period doubling and the quasiperiodic routes to chaos and seems to be somewhat analogous to hydrodynamic systems such as Benard-Rayleigh convection. Chaotic dynamics has been predicted for simple theoretical models of plasmas, e.g., three nonlinearly coupled modes [33].

3.1 Plasma system and models [31]. Figure 22 shows the experimental arrangement: a rod of Ge is placed in parallel electric E and magnetic B fields and cooled to 77°K. Electrons and holes are produced either by laser pumping or by injecting contacts, creating a plasma of density $n_e \approx n_h \approx 10^{13}$ cm^{-3}. As the current I_{dc} is increased by increasing the dc drive voltage V_0, spontaneous current oscillations I(t) are observed [34], attributed to a helical plasma density wave [35], shown schematically in Fig. 22 and believed to be similar to that in gas plasmas [36].

For times and distances of interest, the following partial differential equations describe the motion of conduction electrons and holes in the crystal [35]:

$$\vec{J}_{e,h} = nq\mu_{e,h}\vec{E} \pm qD_{e,h}\nabla n_{e,h} \pm \mu_{e,h}\vec{J}_{e,h} \times \vec{B} \qquad (15a)$$

$$\frac{\partial n_{e,h}}{\partial t} = \pm\frac{1}{q}(\nabla \cdot \vec{J}_{e,h}) + \gamma \tag{15b}$$

$$\nabla \cdot \vec{E} = -q(n - p)/\varepsilon \tag{15c}$$

where $\vec{J}_{e,h}$ is the electron (hole) current density, q is the magnitude of the electronic charge, μ is the mobility, D is the diffusion constant, ε is the dielectric constant of the sample, γ is the net carrier generation rate. At surfaces perpendicular to the applied electric field, these equations are subject to the boundary condition $J_e = J_h = qsn$, where s is the surface recombination rate. By expanding the carrier densities and the electric field about their equilibrium values [$n = n_0 + n_1(t)$, $p = p_0 + p_1(t)$, $\vec{E} = \vec{E}_0 - \nabla\psi_1(t)$], and substituting these expressions into Eqs. (15), it has been shown [35] that the first order terms lead to a helical density wave, $\rho_1 \cong n_1 = N_1(r)\exp[i\omega t - ikz - im\phi]$ and $\psi_1 = \psi_1(r)\exp[i\omega t - ikz - im\phi]$; m is an integer. Beyond certain thresholds of the applied electric and magnetic fields, this helical density wave is absolutely unstable [$\mathrm{Im}(\omega) < 0$] and spontaneous oscillations occur coincident with the onset of nonlinear behavior.

To incorporate nonlinear behavior into a model which explains the observed chaotic dynamics, we consider a *superposition* of waves in which the time dependence is not assumed to be periodic,

$$n_{h1} \cong n_{e1} = \sum_{k,m} C_{km}(t)N_{km}(r)e^{-ikz-im\phi} + \text{c.c.} \tag{16a}$$

$$\psi_1 = \sum_{k,m} C_{km}(t)\psi_{km}(r)e^{-ikz-im\phi} + \text{c.c.} \tag{16b}$$

resulting in a partial differential equation of the form

$$\partial C_{km}/\partial t = M_{km}C_{km} + \sum_{\substack{k_1,k_2:k_1+k_2=k \\ m_1,m_2:m_1+m_2=m}} M'_{k_1k_2m_1m_2} C_{k_1m_1} C_{k_2m_2} \tag{17}$$

$$+ \sum_{\substack{k_1,k_2:k_1-k_2=k \\ m_1,m_2:m_1-m_2=m}} M'_{k_1k_2m_1m_2} C_{k_1m_1} C^*_{k_2m_2}$$

where M and M' are independent of time, and only M is complex. This equation describes a wave-wave interaction in which a wave with wave vector k can couple nonlinearly to many different pairs of waves (k_1,m_1), (k_2,m_2). It turns out that a special case of Eq. (17) had been considered by Wersinger et al. [33] who studied numerically the evolution of an undamped wave coupled bilinearly to two damped waves:

$$\frac{\partial C_1}{\partial t} = \gamma_1 C_1 + MC_2C_3\exp(-i\delta t) \tag{18a}$$

$$\frac{\partial C_{2,3}}{\partial t} = \gamma_{2,3}C_{2,3} - MC_1C^*_{3,2}\exp(i\delta t) \tag{18b}$$

For $\gamma_2 = \gamma_3$ and $\Gamma \equiv |\gamma_2|/\gamma_1$ they found that C_1 undergoes a period doubling cascade to chaos as Γ is increased. The computed Poincaré section can be reduced to a unimodal return map. It seems that these equations may also exhibit a Hopf bifurcation but no numerical solutions are yet available.

3.2 Experimental results and interpretation [31]. The system of Fig. 22 was found to exhibit a period doubling route and also a quasiperiodic route depending mainly on the control parameters V_0 and $|B|$, as well as the angle between $\vec{B}$ and the rod axis. Fig. 23(a)

shows the measured oscillatory current $I(t)$; the phase portrait $V(t)$ vs. $I(t)$ where $V(t)$ is the potential difference across the end contacts; and the power spectrum $|I(\omega)|^2$. As V_0 is increased, the oscillations show a period doubling sequence to chaos, Fig. 23(d), characterized by a broad-band spectrum, and then to a wide period 3 window. The bifurcation diagram of Fig. 24 shows this behavior as well as higher periodic windows and a return to period 1. The oscillation frequency $f_0 \approx 10^5$ Hz and is determined mainly by E, B, and sample geometry. For different parameter values, a Hopf bifurcation to quasiperiodicity is observed, characterized by a threshold for the appearance of a second (incommensurate) frequency f_2. The power spectrum, Fig. 25, shows two well defined frequencies f_1 ($= f_0$ in Fig. 23) and f_2, together with combination frequencies. The Poincaré sections, Fig. 26, for increasing values of V_0 show behavior characteristic of breakup of the invariant section of a 2-torus, similar to those of Figs. 16 and 17 for coupled p-n junctions.

The fractal dimension d was measured [31] for the attractor of Fig. 26(d), with the preliminary average value $d \approx 2.65$. This was obtained by the method of Brandstater et al. [21], as follows.

A data set of $q = 98{,}000$ successive values of the local current maxima of $I(t)$ was recorded using a peak detector, a fast 12-bit analog-to-digital converter, and a LSI-11/23 computer. From these data a D-dimensional phase space was reconstructed [13]. In this reconstructed space the number of points $N(\varepsilon)$ on the attractor which are contained in a D-dimensional hypersphere of radius ε should scale as $N(\varepsilon) \propto \varepsilon^d$. We measure $N(\varepsilon)$ for many hyperspheres on the attractor, calculate the average $\overline{N(\varepsilon)}$, and plot $\log \overline{N(\varepsilon)}$ vs. $\log \varepsilon$.

The slope of this plot, for small ε, is the dimension d. Figure 27 shows results for three values D = 2, 4, and 8. The slope is seen to converge for $D \geq 4$ to 1.65 for this Poincaré section, implying d = 2.65 for the complete attractor. For small values of ε there is a break to a steeper slope, which increases with embedding dimension and is due to random noise in the signal. This method of data analysis can thus discriminate between high dimensional random processes and lower dimensional deterministic chaos, as noted by Ben-Mizracki, Procaccia, and Grassberger [36b].

To summarize, spontaneous plasma current oscillations in Ge crystals are found to exhibit a period doubling cascade to chaos and the quasiperiodic route to chaos. This is the first reported observation of chaotic dynamics in any plasma and can be qualitatively understood from nonlinear wave-wave coupling. This is a good system for study of quasiperiodicity, and may show higher dimensional, more turbulent behavior, and breakdown of spatial order. A more rigorous understanding is desirable, possibly from solution of the partial differential equations.

4. SPIN WAVES IN FERRITE SPHERES

It was discovered that ferromagnetic resonance in some ferrites displays premature saturation and subsidiary resonance when excited above a critical value of the rf driving field H_1 [37]. This was explained by Suhl [38], who developed a detailed theory of nonlinear coupling between the uniform precession mode of the magnetization vector and spin waves. He showed that the uniform precession could excite spin waves, whose amplitude grows essentially exponentially at a critical value of H_1. He wrote [38] "...this situation bears a certain resemblance to the turbulent state in fluid dynamics...".

The subsequent observation of low frequency (10^4 to 10^6 Hz) noisy "auto-oscillations" of the magnetization [39,40] was believed to be due to excitation of spin waves but not fully understood. From the more recent perspective of nonlinear dynamics theory, one is tempted to interpret these experimental results as examples of chaotic dynamics. To this end we have experimentally reexamined the auto-oscillations in spheres of yttrium iron garnet (YIG), and have observed period doubling bifurcations, onset of chaos, and periodic windows [41]. Similar chaotic dynamics has been predicted for a related phenomenon, the parallel pumping of a ferromagnet [42].

4.1 Spin system and models. Figure 28 shows the experimental arrangement used: a Ga-doped YIG sphere of radius R is wound with a pick-up coil and a driving coil at right angles, providing a field H_1 at the sphere from an oscillator of frequency f_o and variable voltage V_{rf}. This assembly is mounted in a magnetic field H_{dc} along a third, mutually perpendicular axis, which provides the Zeeman field for ferromagnetic resonance, observed from the voltage V_s induced into the pick-up coil by the sample magnetization $\vec{M}(t)$, precessing about H_{dc}. To observe auto-oscillations of M(t) we observe $V_s(t)$ at some fixed value of H_{dc} near its resonance value. The Ga-YIG spheres were highly spherical and highly polished. Typical parameters used are: radius R = 0.047 cm; saturation magnetization $4\pi M_s$ = 300 gauss; f_o = 1.3 GHz; $H_{dc} \cong 460$ gauss; resonance line width $\simeq$ 0.5 gauss. Experiments were done at room temperature and with the perpendicular pumping configuration ($\vec{H}_1 \perp \vec{H}_{dc}$) of Fig. 28. Although parallel pumping ($\vec{H}_1 \parallel \vec{H}_{dc}$) was attempted, no

chaotic dynamics were observed, possibly because of insufficient pumping power available.

For a set of spins $\vec{S}_j$ on a lattice in an external magnetic field $\vec{H}_o$, an appropriate Hamiltonian is [43]

$$\mathcal{H} = \gamma\hbar\sum_j \vec{H}_o\cdot\vec{S}_j - \left(\frac{D}{Sa^2}\right)\gamma\hbar\sum_j \vec{S}_j\cdot\vec{S}_{j+1} + \mathcal{H}_{dd} \tag{19}$$

The first term is the Zeeman interaction (γ = gyromagnetic ratio); the second is the Heisenberg exchange interaction (D = exchange constant; a = lattice spacing); the last term is the dipole-dipole interaction. The Zeeman interaction gives rise to a uniform precession of the sample magnetization $\vec{M}$ about $\vec{H}_o$ at $\omega_o = \gamma H_o$ for a spherical sample. The second term leads to spin waves of frequency ω_k and wave vector k, described by the dispersion relation [44]

$$\omega_k^2 = \left[\omega_o - \frac{\omega_M}{3} + \gamma Dk^2\right]\left[\omega_o - \frac{\omega_M}{3} + \gamma Dk^2 + \omega_M \sin^2\Theta_k\right] , \tag{20}$$

valid for a sphere, with spin waves propagating in a direction $\hat{k}$ at angle Θ_k to $\vec{H}$; here $\omega_M = \gamma 4\pi M_s$. For the values $\omega_o = 8.16 \times 10^9$ sec^{-1}, $\omega_M = 5.27 \times 10^9$ sec^{-1}, $\gamma = 17.58 \times 10^6$; $D = 5.4 \times 10^{-9}$ Oe cm^2 used in our experiment, ω_k is plotted in Fig. 29 for three angles: $\Theta = 0$, $\Theta = 90°$, and $\Theta = \Theta_o = 60.4°$, the value for which $\omega_o = \omega_k$ at $k = 0$; this is the largest angle for which ω_o can equal ω_k. It is the nonlinear coupling between the uniform mode at ω_o and spin waves at ω_k that gives rise to the instabilities of interest, chiefly through the dipolar term.

Suhl analyzed this system from first principles finding the differential equations of motion including the leading nonlinear

terms for the evolution of the dynamical variables a_o, a_k, and a^*_{-k}, the amplitudes of the uniform mode (k=0) and spin waves of wave vector k and -k, respectively. Very approximately, these can be written as

$$\dot{a}_o = \beta a_o - k a_o + O(a_k \cdot a^*_{-k}) \tag{21a}$$

$$\dot{a}_k = A_k a_k + B_k A^*_{-k} + O(a_o \cdot a_k) + O(|a_o|^2 \cdot a_k) \tag{21b}$$

and its adjoint.

The experimental conditions for instabilities arising from the nonlinear terms of order $a_o a_k$ in Eq. (21b) are not satisfied by our parameters. However the term $O(|a_o|^2 \cdot a_k)$ gives rise to Suhl's second order instability through saturation of the main resonance: $\omega_o = \omega_k$, $H_{res} = H_o$. The lowest threshold value of H_1 occurs at $\Theta_k = 0$ in Eq. 20, corresponding to $\gamma D_{k_1}^2 = \omega_M/3$, i.e. to the value k_1 shown in Fig. 29. This means that as the main ferromagnetic resonance is saturated by increasing H_1, the first instability will excite spin waves (ω_k, k), which will travel along H_o in the sphere.

Because of the finite line width of the resonance, spin waves of spread $\Delta\omega_k$ and Δk will be excited, and can be described as a spin wave packet with group velocity $v_g = d\omega_k/dk$, which can be found from Eq. (20). Standing-wave modes of this packet can be set up in the sphere, the lowest normal mode corresponding to [40]

$$\omega_A = \Delta k \cdot v_g = \pi v_g/R \tag{22}$$

Oscillations at ω_A should be manifest experimentally as a time modulation of the signal voltage V_s. One concludes that rf excitation at frequency $\omega_o \simeq 10^9$ sec^{-1} will generate auto-oscillations of the

magnetization at $\omega_A \approx 10^5$ sec^{-1}, this frequency being determined by the radius of the sphere and the microscopic parameters of the magnetic system D, M_s, γ. In some sense this is analogous to the excitation of convection loop frequencies in a fluid driven by a temperature gradient in Bénard-Rayleigh convection.

4.2 Experimental results and interpretation. Figure 30 is a series of ferromagnetic resonance line shapes for increasing values of the driving field H_1 showing low power unsaturated resonance, broadening and premature saturation, onset of instability and noisy oscillations, and more fully developed oscillations. These auto-oscillations have a well defined H_1 for their onset. Figure 31(a) shows the oscillations observed at the lowest value of H_1 at frequency $f_{A1} \approx 250$ kHz. As H_1 was increased, these diminished in amplitude; other auto-oscillations as in Fig. 31(b) at the frequency $f_{A2} \approx 16$ Khz were observed at higher H_1 [cf. Fig. 30(d)]. We interpret f_{A1} and f_{A2} as follows. The lowest frequency mode will be given by Eq. (22), which for radius R = 0.047 cm and $v_g(\Theta=0)$ gives $f_A = \omega_A/2\pi = \sqrt{\gamma D \omega_M/3}/R = 275$ kHz, which corresponds favorably with observed f_{A1}. The low frequency oscillations at f_{A2} cannot be due to a higher order mode at $\Theta = 0$, and we ascribe them to the zero order mode of Eq. (22) but with a small value of v_g at some angle Θ^* such that $f_{A2} = \omega_A/2\pi = v_g(\Theta^*)/2R$, which requires $v_g = 1.5 \times 10^3$ cm/sec, which can be obtained for $\Theta = \Theta^* = 60°$, i.e., close to the value $\Theta_0 = 60.4°$ at which $k \to 0$, Fig. 29. We postulate that the strong auto-oscillations at f_{A2} are due to the lowest order spherical Bessel function mode of a packet of spin waves of wave

vector $k \approx 0$. These oscillations were found to show chaotic dynamics. This is shown most simply by the sequence of f_{A2} oscillation signals, Fig. 31, obtained at increased H_1 values. These first appear in Fig. 31(b) as a sine wave. There is a higher threshold at which the signal bifurcates to period 2, then to period 4. Further increase of H_1 leads to onset of a "noisy" aperiodic signal we call chaos, Fig. 32(a), although we have not proved experimentally that it is deterministic. However, the observed power spectrum is broad band, and there is no reason why random (e.g., thermal) noise should so abruptly increase. We also observed a periodic state of period 3, Fig. 32(b), which bifurcates to period 6, Fig. 32(c), and then becomes chaotic. Other periodic states observed are period 5 and period 4, Fig. 32(d), with a visitation pattern different from that of Fig. 31(d). Although the overall behavior seems roughly similar to that observed in, say, a p-n junction, the spin system is less stable and the behavior less reproducible. There are more parameters (H_0, f_0, H_1, crystal orientation, temperature) that can fluctuate. This gives the appearance of intermittency, however probably not that of Manneville and Pomeau. We also observe a strong hysteresis, i.e., a dependence of the chaotic dynamics on the direction in which H_0 and f_0 are set to resonance, and also on whether H_1 is increased or decreased toward a threshold value. The system seems to have several attractors with quite different behavior. That described above is probably the most characteristic and reproducible. Another, quite different, signal shape is also observed, reminiscent of relaxation oscillations in general. We believe that these are distinct phenomena but have not investigated their possibly chaotic dynamics.

Power spectra were measured by a frequency scanning spectrum analyzer, with results confirming the signal periods measured above from real time analysis. The chaotic state, Fig. 32(a), showed a wide band spectrum with a broad peak at f_{A2}. By plotting $V_s(t)$ vs. $\dot{V}_s(t)$ on an oscilloscope, real time phase portraits were observed.

From a time sample of $V_s(t)$ a return map $V_s(t+\tau)$ vs. $V_s(t)$ was constructed, with $\tau \simeq 0.2$ T; the shape was roughly unimodal, with considerable scatter in the data points. At other parameter values of the system return maps were generated by plotting $V_s(t+T)$ vs. $V_s(t)$ directly on an oscilloscope using a zero-crossing detector to give a strobing pulse train of approximate period T. These showed periodic attractors 1, 2, 4 ..., 3, 6, as well as circular and elliptical shapes. They can be fit, but not necessarily uniquely, by the Henon map, Eq. (7), with B = 1, corresponding to very small dissipation. This is consistent with the observation that the spin wave mode at f_{A2} had a very long lifetime, $\sim 10^3$ cycles. We consider these preliminary results, however, and point out that more work is necessary: a numerical solution of the full equations [e.g. Eq. (21)] and computation of Poincaré sections; more data, preferably at higher frequencies and fields; search for quasiperiodicity, which seems likely for this system; and parallel pumping experiments.

5. SUMMARY AND CONCLUSIONS

A driven p-n junction is found to display in the simplest case a clear period doubling route to chaos; a period adding route (frequency locking) when driven harder; intermittency;

and hysteresis. All this behavior can be understood from first principles by numerical solution of the governing differential equations; the Poincaré section is a map of the plane.

For N=2 coupled driven junctions, in addition to the above, a Hopf bifurcation to a two-frequency quasiperiodic state is observed, with entrainment horns, intermittency, hysteresis, and chaos. Bifurcation diagrams show complex intertwining of period doubling, locking, and double periodicity. The behavior can be moderately understood by solution of the differential equations, and is also qualitatively modeled by two coupled maps of the plane or, for large dissipation, by two coupled one-dimensional maps. For N=12 coupled p-n junction, additional Hopf bifurcation is observed, up to a four-frequency quasiperiodic state.

Spatio-temporal electron-hole plasma wave oscillations in a crystal of Ge show period doubling and two-frequency quasiperiodicity. The period doubling is understandable from numerical solution of model differential equations. This seems to be a good system for detailed study of the quasiperiodic route. Spin wave instabilities in ferrite spheres show a period doubling route to chaos and deserve to be more fully studied experimentally and theoretically.

Mere observation of some recognizable routes to chaos in a system is certainly not a solution to the problem, and we have tried to indicate why specific observed behavior arises from first principles, but this is only the beginning. To achieve a predictive understanding of instabilities in solids one can start with the (usually well known) governing differential equations; use dynamical variables

accessible to measurement; include the parameters Λ of the physical system; compute a numerical solution for a given set Λ, and a Poincaré section. For sufficient dissipation one expects this section to be a low dimensional map with a few parameters λ; qualitative behavior can thus be quickly explained, or even already known, if the map has a recognizable form previously studied. However, detailed understanding requires the relations between the physical parameters Λ and the map parameters λ. Herein lies the problem in using maps as models; to numerically establish the form of the Λ,λ relationship would be a step forward. Chaotic dynamics theory has much to contribute to understanding solid state instabilities. Likewise, solid state systems are often well characterized, have low extrinsic (random) noise, a wide range of behavior, and are good systems from the viewpoint of a nonlinear dynamicist interested in physical reality.

Acknowledgments

I acknowledge with much thanks the large contributions to this work by my students: Paul Bryant, Robert Van Buskirk, George Gibson, Glenn Held, Jose Perez, and James Testa. Informative discussions with J. P. Crutchfield, M. Nauenberg, B. A. Huberman, A. N. Portis, R. M. White, and R. M. Westervelt are also gratefully acknowledged. I wish to thank the Miller Institute for Basic Research in Science for a Research Professorship. This work was supported by the Director, Office of Energy Research, Office of Basic Energy Sciences, Materials Sciences Division of the U.S. Department of Energy under Contract Number DE-AC03-76SF00098.

References

[1] Feigenbaum, M. J., J. Stat. Phys. 19, 25 (1978).

[2] Eckmann, J.-P., Rev. Mod. Phys. 53, 643 (1981).

[3] Linsay, P. S., Phys. Rev. Lett. 47, 1349 (1981); Testa, J., Perez, J., Jeffries, C., Phys. Rev. Lett. 48, 714 (1982); Perez, J., Thesis, 1983, Univ. of Calif., Berkeley (Lawrence Berkeley Laboratory Report LBL-16898); Rollins, R. W. and Hunt, E. R., Phys. Rev. Lett. 49, 1295 (1982); Hunt, E. R. and Rollins, R. W., Phys. Rev. A 29, 1000 (1984); Ikezi, H., deGrassie, J. S., and Jensen, T. H., Phys. Rev. A 28, 1207 (1983); Brorson, S. D., Dewey, D., and Linsay, P. S., Phys. Rev. A 28, 1201 (1983).

[4] See, e.g., Kaplan, A. E., Radio Engineering and Electronic Physics 9, 1424 (1964), and references therein.

[5] Jeffries, C. and Perez, J., Phys. Rev. A 26, 2117 (1982).

[6] Perez, J. and Jeffries, C., Phys. Rev. B 26, 3460 (1982).

[7] Jeffries, C. and Wiesenfeld, K., submitted for publication.

[8] Grebogi, C., Ott, E., and Yorke, J. A., Phys. Rev. Lett. 48, 1507 (1982); Jeffries, C. and Perez, J., Phys. Rev. A 27, 601 (1983).

[9] Rollins, R. W. and Hunt, E. R., Phys. Rev. A, to be published.

[10] Van Buskirk, R. and Jeffries, C., to be published.

[11] Van Buskirk, R., Thesis, 1984, Univ. of Calif., Berkeley (Lawrence Berkeley Laboratory Report LBL-17868).

[12] See, e.g., Wang, S., Solid State Electronics, Ch. 6, McGraw-Hill Publishing Co., New York, 1966.

[13] Packard, N. H., Crutchfield, J. P., Farmer, J. D., and Shaw, R. S., Phys. Rev. Lett. 45, 712 (1980).

[14] See, e.g., Rossler, O. E., Z. Naturforsch. 31a, 259 (1976).

[15] Conte, S. D. and deBoor, C., Elementary Numerical Analysis, p. 32, McGraw-Hill Publishing Co., New York, 1980.

[16] Ott, E., Rev. Mod. Phys. 53, 655 (1981).

[17] Swift, J. and Wiesenfeld, K., Phys. Rev. Lett. 52, 705 (1984).

[18] May, R. M., Nature (London) 261, 459 (1976).

[19] Henon, M., Comm. Math. Phys. 50, 69 (1976).

[20] Mandelbrot, B. B., The Fractal Geometry of Nature, Freeman Press, San Francisco, 1982.

[21] Farmer, J. D., Ott, E., and Yorke, J. A., Physica 7D, 153 (1983); Brandstater, A. et al., Phys. Rev. Lett. 51, 1442 (1983).

[22] Held, G., private communication.

[23] See, e.g., Jordan, D. W. and Smith, P., Nonlinear Ordinary Differential Equations, Ch. 7, Clarendon Press, Oxford, 1977.

[24] Guckenheimer, J. and Holmes, P., Nonlinear Oscillations, Dynamical Systems and Bifurcations of Vector Fields, Springer Verlag, New York, 1983.

[25] Shenker, S. J., Physica 5D, 405 (1982); Feigenbaum, M. S., Kadanoff, L. P., and Shenker, S. J., Physica 5D, 370 (1982); Ostlund, S., Rand, D., Sethna, J., and Siggia, E., Physica 8D, 303 (1983).

[26] Bryant, P. and Jeffries, C., Lawrence Berkeley Laboratory Report LBL-16948, Jan. 1984; short version to be published in Phys. Rev. Lett., July 16, 1984.

[27] Arnold, V. I., Trans. Am. Math. Soc. 2nd Series 46, 213 (1965); see also ref. 24, Ch. 7 and Glass, L. and Perez, R., Phys. Rev. Lett. 48 (1982), Fig. 2.

[28] Hogg, T. and Huberman, B. A., Phys. Rev. A 29, 275 (1984), Fig. 6.

[29] Curry, J. H. and Yorke, J. A., Lecture Notes in Math. 688, 48 (1978); Froyland, J., Physica 8D, 423 (1983); Gu, Y. et al., Phys. Rev. Lett. 52, 701 (1984); Kaneko, K., Prog. Theor. Phys. (Japan) 69, 1427 (1983); Yuan, J. M. et al., Phys. Rev. A 28, 1662 (1983).

[30] See, e.g., Hartnagel, H., Semiconductor Plasma Instabilities, Elsevier Publishing Co., New York, 1969.

[31] Held, G., Jeffries, C. and Haller, E. E., Phys. Rev. Lett. 52, 1037 (1984); Held, G., Jeffries, C., and Haller, E. E., Proceedings of the 17th International Conference on Physics of Semiconductors, 1984, Springer Verlag, New York, to be published.

[32] Teitsworth, S. W. and Westervelt, R. M., Phys. Rev. Lett. 51, 825 (1983).

[33] Wersinger, J.-M., Finn, J. M., and Ott, E., Phys. Fluids 23, 1142 (1980).

[34] Ivanov, I. L. and Ryvkin, S. M., Zh. Tekh. Fiz. 28, 774 (1958) [Sov. Phys. Tech. Phys. 3, 722 (1958)]; Larrabee, R. B. and Steele, M. C., J. Appl. Phys. 31, 1519 (1960); Boh, J. and Veilex, R., Compt. Rend. 248, 2300 (1958).

[35] Glicksman, M., Phys. Rev. 124, 1655 (1961); Hurwitz, C. E. and McWhorter, A. L., Phys. Rev. 134, A1033 (1964).

[36] Kadomtsev, B. B. and Nedospasov, A. V., J. Nucl. Energy 1, 230 (1960); Hoh, F. C. and Lehnert, B., Phys. Rev. Lett. 7, 75 (1961).

[36b] Ben-Mizracki, A., Procaccia, I., and Grassberger, P., Phys. Rev. A29, 975 (1984).

[37] Damon, R. W., Rev. Mod. Phys. 25, 239 (1953); Bloembergen, N., and Wang, S., Phys. Rev. 93, 72 (1954).

[38] Suhl, H., J. Phys. Chem. Solids 1, 209 (1957).

[39] Hartwick, T. S., Peressini, E. R. and Weiss, M. T., J. Appl. Phys. 32, 223S (1961); for a review of the extensive Soviet work on spin wave instabilities, see Zakharov, V. E., L'vov, V. S., and Starobinets, S. S., Usp. Fiz. Nauk. 114, 609 (1974) [Sov. Phys.-Usp. 17, 896 (1975)].

[40] Wang, S., Thomas, G., and Hsu, T., J. Appl. Phys. 39, 2719 (1968); Thomas, G. and Komoriya, G., J. Appl. Phys. 66, 883 (1975).

[41] Gibson, G. and Jeffries, C., Phys. Rev. A 29, 811 (1984).

[42] Nakamura, K., Ohta, S., and Kawasaki, K., J. Phys. C: Solid State Phys. 15, L143 (1982); Ohta, S. and Nakamura, K., J. Phys. C: Solid State Phys. 16, L605 (1983).

[43] See, e.g., Kittel, C., Intro. to Solid State Physics, Wiley Publishing, 1976, Ch. 15, 16.

[44] Clogston, A. M., Suhl, H., Waller, L. R., and Anderson, P. W., J. Phys. Chem. Solids 1, 129 (1957).

Figure Captions

Fig. 1 - A p-n junction in a silicon crystal, resonantly driven by a voltage $V_o(t)$ through an inductance L and resistance R. The observed dynamical variables are the current I and potential difference V. Additional junctions may be connected between A and C or B and C.

Fig. 2 - Observed bifurcation diagram for driven p-n junction consecutive current maxima $\{I_n\}$ vs. drive voltage V_{os} (horizontal axis), showing cascade of period doubling to chaos, band merging, period 5 and period 3 window with hysteresis. f = 3.87 kHz, L = 470 mH, R = 244 Ω, 300A p-n junction.

Fig. 3 - Power spectra of driven p-n junction at consecutive values of drive voltage $V_o(t)$ RMS. (a) 1.040; (b) 1.330; (c) 1.488; (d) 1.601; (e) 2.887. Relative frequency 1.0 corresponds to 20 kHz; L = 100 mH, R = 53 Ω, 1N4723 p-n junction.

Fig. 4 - (a) Bifurcation diagram $\{I_n\}$ vs. drive voltage V_{os} for p-n junction showing period doubling and period adding (frequency locking). (b) Average junction current $\bar{I}$ vs. V_{os}, showing peaks at frequency locking regions. f = 28 kHz, L = 10 mH, R = 8 Ω, 300A p-n junction.

Fig. 5 - Shaded areas show observed locking regions N:1 in parameter space for the period adding region of bifurcation diagram, e.g., Fig. 4. L = 10 mH, R = 8 Ω, 1N4721 p-n junction.

Fig. 6 - Oval lines: $I(t)$ vs. $\dot{I}(t)$ (horizontal axis) for one band chaos in driven p-n junction. This is a projection of the strange attractor. Dark line: a strobed Poincaré section of the attractor. f = 100 kHz, L = 10 mH, R = 100 Ω, 1N4004 p-n junction [Ref. 3, J. Perez, Thesis].

Fig. 7 - (b) Observed 3-dimensional return map of driven p-n junction. (a) Computed return map from Henon equation [Eq. (7)] with A = 1.5, B = 0.08. (c) Observed 3-dimensional return map for chaotic region between period 4 and 5 in Fig. 4.

Fig. 8 - High resolution Poincaré section $(\dot{I},I)$, showing self-similarity and fractal structure. f = 76 kHz, L = 10 mH, R = 43 Ω, 1N4721 p-n junction.

Fig. 9 - Observed phase diagram for driven p-n junction, showing boundaries between periods 1, 2, 4, 8; threshold for chaos; C2 = two-band chaos; C1 = one-band chaos; period 3, 6, C3 = three-band chaos; C1 = one-band chaos; hysteresis (↑,↓); and 1:1 bifurcation. L = 100 mH, R = 53 Ω, 1N4723 p-n junction.

Fig. 10 - Bifurcation diagram, $X(J) = \{q\}$ vs. A_0, computed from Eq. (3) with $a(q) \rightarrow a = 0.45$ and $\omega = 1$, showing characteristic period doubling to chaos and period 3 window with hysteresis.

Fig. 11 - Bifurcation diagram $X(J) = \{x_n\}$ vs. A_0 computed from Eq. (9) with B = 0.1, showing period doubling, period adding, and hysteresis, with overall behavior similar to data, Fig. 4(a).

Fig. 12 - Transient recovery time τ vs. drive voltage V_{os} near $1 \rightarrow 2$ period doubling, showing critical slowing down phenomena. Roughly, $\tau \propto |V_{os}-V_{cr}|^{-0.8}$ with V_{cr} = 603 mV. L = 470 mH, R = 244 Ω, f = 3.87 kHz, 300A p-n junction.

Fig. 13 - (a) Observed bifurcation diagram $\{I_n\}$ vs. V_{os} (horizontal) for two resistively coupled p-n junction resonators, showing period doubling, Hopf bifurcation to quasiperiodicity; entrainment at period 18; doubling to period 36; chaos; and crisis. (b) Bifurcation diagram $\{V_n\}$ vs. V_{os} at top center section of (a), showing more clearly Hopf bifurcation, entrainment, doubling, chaos. f_1 = 27 kHz, R = 1200 Ω, L = 100 mH, 1N4723 p-n junction.

Fig. 14 - Phase diagram for quasiperiodic region for two coupled p-n junctions, of Fig. 13, showing the Hopf bifurcation boundary; entrainment horns; period doubling to chaos (c); and large domain of chaos within the dashed parabola. The entrainment horns labeled by N/2 = 7, 16, 25, 9, and 11 correspond to rotation numbers (M/N) = 3/14, 7/32, 11/50, 4/18, and 5/22, respectively.

Fig. 15 - Sequence of phase portraits $(I,\dot{I})$ and strobed Poincare sections for two inductively coupled p-n junctions with increasing drive voltage V_{os}(rms). (a) 0.946, period 1 orbit; (b) 0.958, Hopf bifurcation to 2-torus; (c) 0.988; (d) 1.015. At 1.021 rms volts, locking to M/N = 1/4 occurs. f = 26.5 kHz, L = 10 mH, 1N4723 p-n junction.

Fig. 16 - Sequence of Poincaré sections (V_1, I_2) showing quasi-periodic route to chaos for two resistively coupled p-n junctions of Fig. 13(b) for increasing drive voltage V_{os}(rms). (a) 3.165, smooth torus just after Hopf bifurcation; (b) 3.681 wrinkled torus; (c) 4.028, more wrinkled; (d) entrainment to M/N = 4/18.

Fig. 17 - Poincaré sections, continuation of Fig. 16. (a) V_{os} = 4.409, period doubling; (b) 4.882, strange "rabbit" attractor; (c) 5.182, folding of attractor; (d) 8.958, more folding, with measured dimension d_c = 2.23, see text.

Fig. 18 - Observed power spectra near $f_1/4$ for same sequence as Figs. 16, 17 for quasiperiodic behavior (of system of Fig. 13) at increasing drive voltage V_{os}(rms). (a) 3.166; (b) 3.681; (c) 4.028; (d) 4.190; (e) 4.409; (f) 4.882 (strange "rabbit" attractor); (g) 5.132; (h) 8.958. On a wider frequency scan there are strong sharp lines (+45 dB) at $f_1/2$, f_1, $3f_1/2$... .

Fig. 19 - Observed Poincaré sections (V_1, I_2) for two resistively coupled p-n junctions at increasing drive voltage V_{os}(rms). (a) 1.542; (b) 1.706; (c) 1.897; (d) 1.951. The orbits oscillate in the corners where periodic attractors will appear at V_{os} = 2.021. f = 28 kHz, R = 510 Ω, L = 100 mH, 1N4723 p-n junction.

Fig. 20 - Bifurcation diagram $X(J) = \{q_n\}$ vs. A_o computed from Eqs. (10) with a = 0.45, β = 0.95, r = 0.6, ω = 1.5.

Fig. 21 - Bifurcation diagram {x} vs. A computed from Eqs. (14) with C = 0.3, b = 0.95.

Fig. 22 - Experimental arrangement for observation of chaotic dynamics of helical plasma wave instability in a germanium rod [31]. Typically, R = 100 Ω, V_0 = 0 to 25V, B = 1 to 15 kG, rod diameter ≃ 0.1 to 0.8 cm, length ≃ 1 cm.

Fig. 23 - Oscillating current I(t), phase portrait V(t) vs. I(t), and power spectra for plasma wave oscillations in a Ge rod (0.1 x 0.1 x 1.0 cm^3, T = 77°K, B = 4.3 kG) for a sequence of increased values of V_0. (a) period 1; (b) period 2; (c) period 4; (d) onset of chaos; (e) period 3 window [31].

Fig. 24 - Bifurcation diagram, $\{I_{max}\}$ vs. V_0, for Ge rod, as in Fig. 23, showing period doubling to chaos (C1); period 3 window W3; chaos (C2); etc., to period 1 at V_0 = 10.65 [31].

Fig. 25 - Power spectrum for plasma wave oscillations in 0.1 x 0.1 x 1.0 cm^3 Ge rod in quasiperiodic mode, showing first oscillatory frequency f_1 and second frequency f_2 arising at Hopf bifurcation, together with combination frequencies.

Fig. 26 - Sequence of return maps, I_{n+1} vs. I_n, for quasiperiodic plasma wave oscillations in Ge rod as in Fig. 25, showing quasiperiodic route to chaos as V_0 is increased, (a) to (d). For (d) the measured fractal dimension d = 2.65.

Fig. 27 - Plot of $\log_2 \overline{N(\varepsilon)}$ vs. $\log_2 \varepsilon$ for a Poincaré section data set of current maxima for plasma wave oscillations, Fig. 26(d), for embedding dimension D = 2, 4, 8. The slope is 1.65 for this Poincaré section. The points below $\log_2 \varepsilon \simeq 5$ are due to high dimensional random noise in the system.

Fig. 28 - Experimental arrangement for observation of spin wave instabilities in ferrite (YIG) sphere in a magnetic field H_{dc}. A rf field H_1 induces uniform precession of the magnetization, which couples nonlinearly to a standing mode of spin wave packets in the sphere [41].

Fig. 29 - Dispersion relation, frequency ω_k vs. wave vector k for spin waves in Ga-YIG sphere used in experiments. First instability occurs at $k = k_1$ where spin wave frequency becomes equal to uniform precession frequency ω_0 (Kittel mode)[41].

Fig. 30 - Observed ferromagnetic resonance line shape of system, Fig. 28, with increased values of drive field H_1. (a) $H_1 = 1$ (relative units); (b) $H_1 = 30$; (c) $H_1 = 31$; (d) $H_1 = 35$, showing fully developed auto-oscillations that have become chaotic [41].

Fig. 31 - Real time signals $V_s(t)$ for auto-oscillations for increasing values of H_1: (a) as in Fig. 30(c), oscillations at $f_{A1} \simeq 250$ kHz; (b) oscillations at $f_{A2} \simeq 16$ kHz; (c) bifurcation to $f_{A2}/2$; (d) bifurcation to $f_{A2}/4$ [41].

Fig. 32 - $V_s(t)$ for auto-oscillations at f_{A1} for increasing H_1: (a) chaos following Fig. 31(d); (b) period 3 window; (c) bifurcation to period 6; (d) period 4 [41].

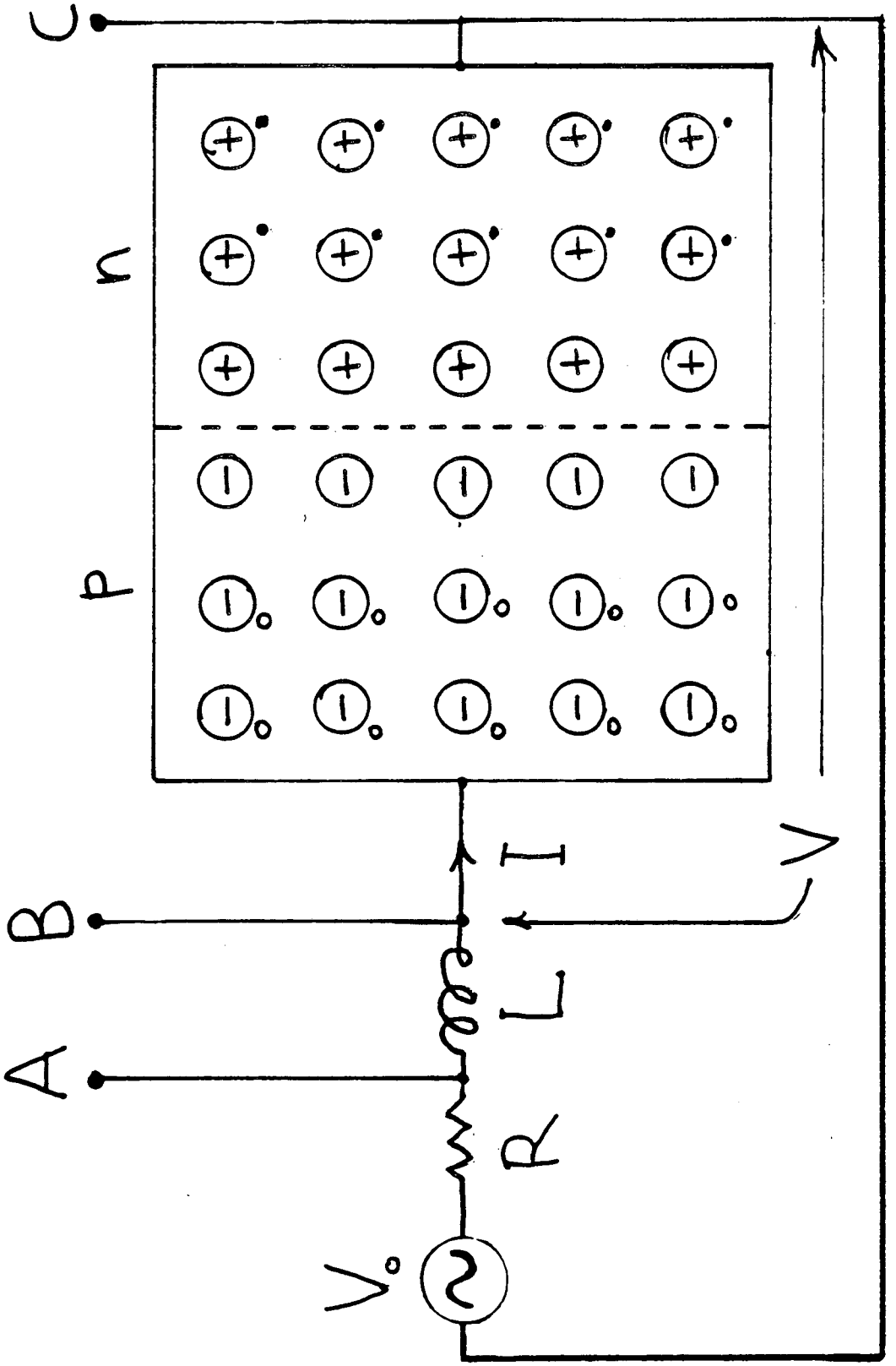

XBL 845-1950

Fig. 1

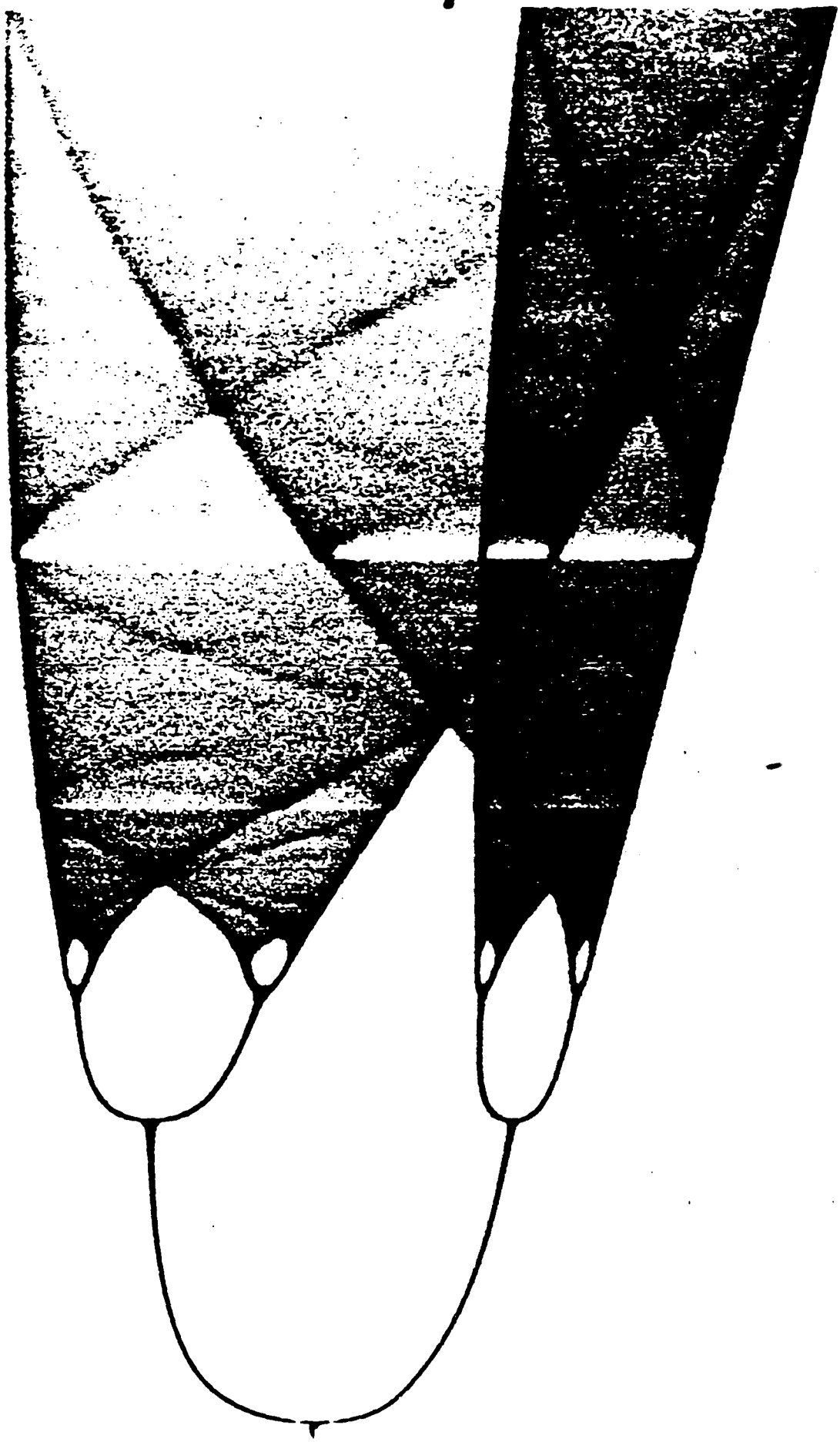

Fig. 2

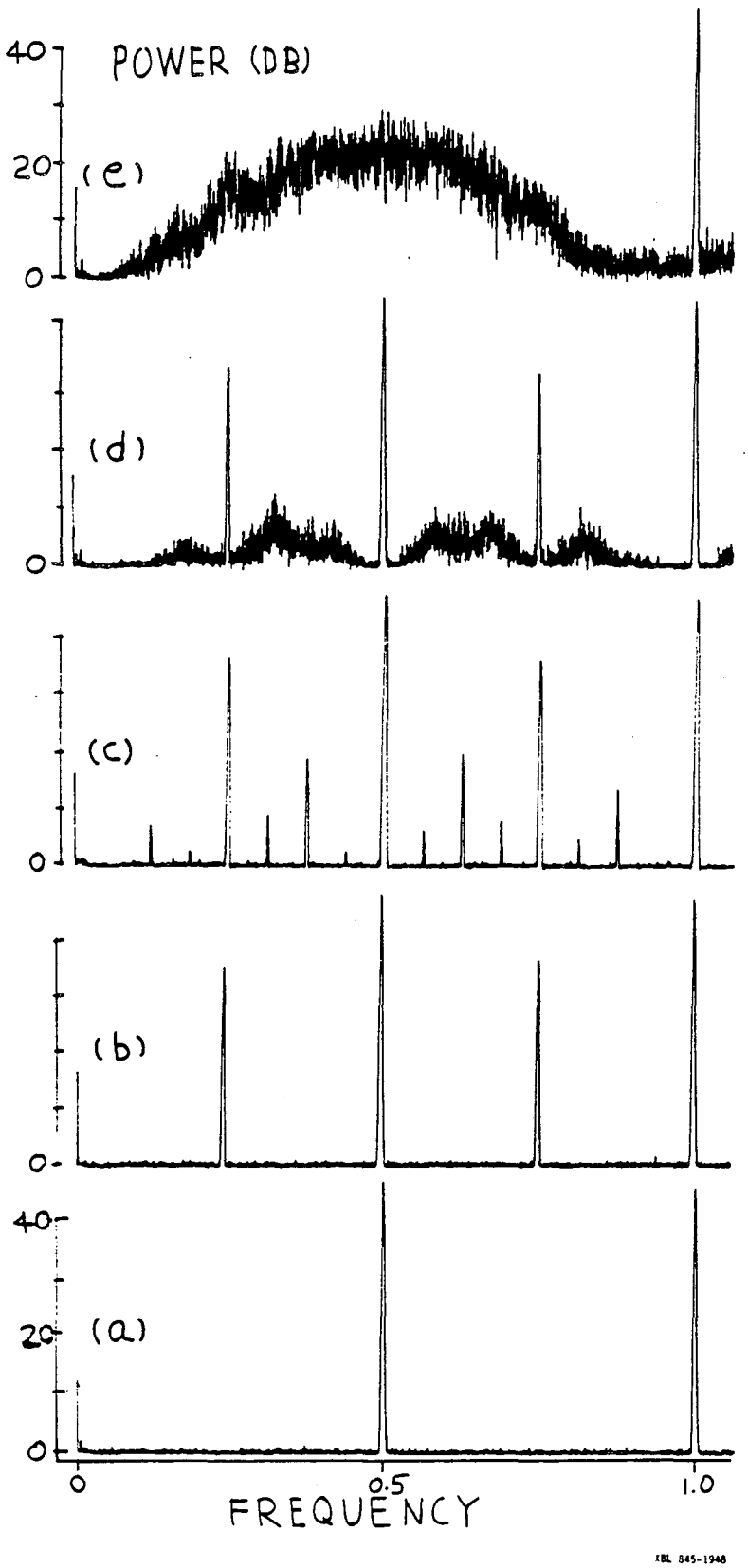

Fig. 3

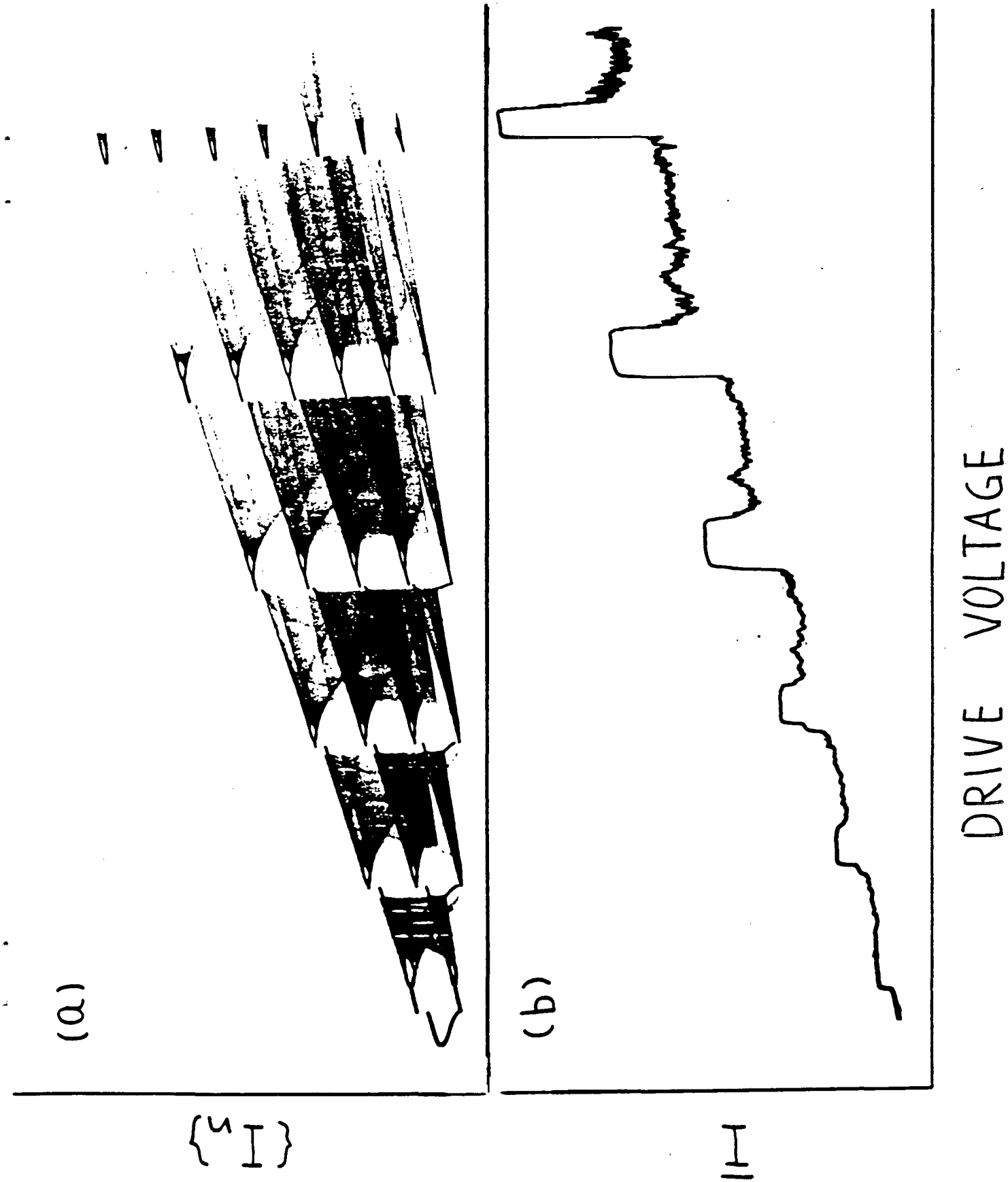

Fig. 4

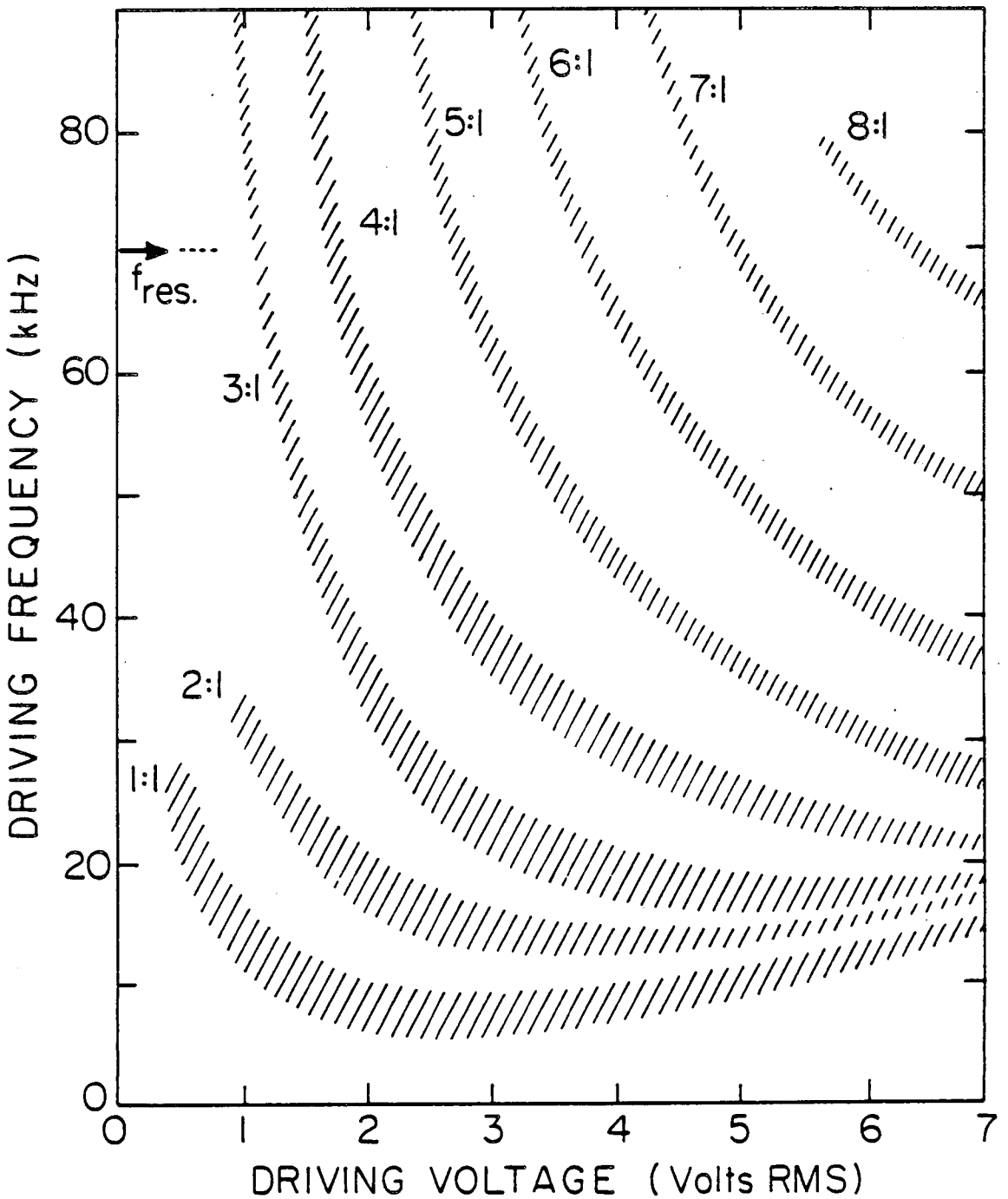

XBL833-5381

Fig. 5

TOP ↑

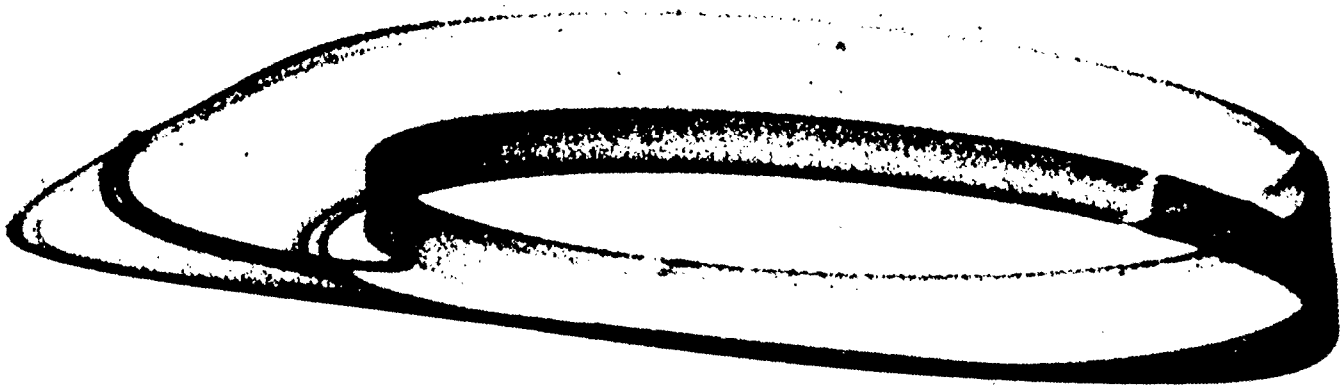

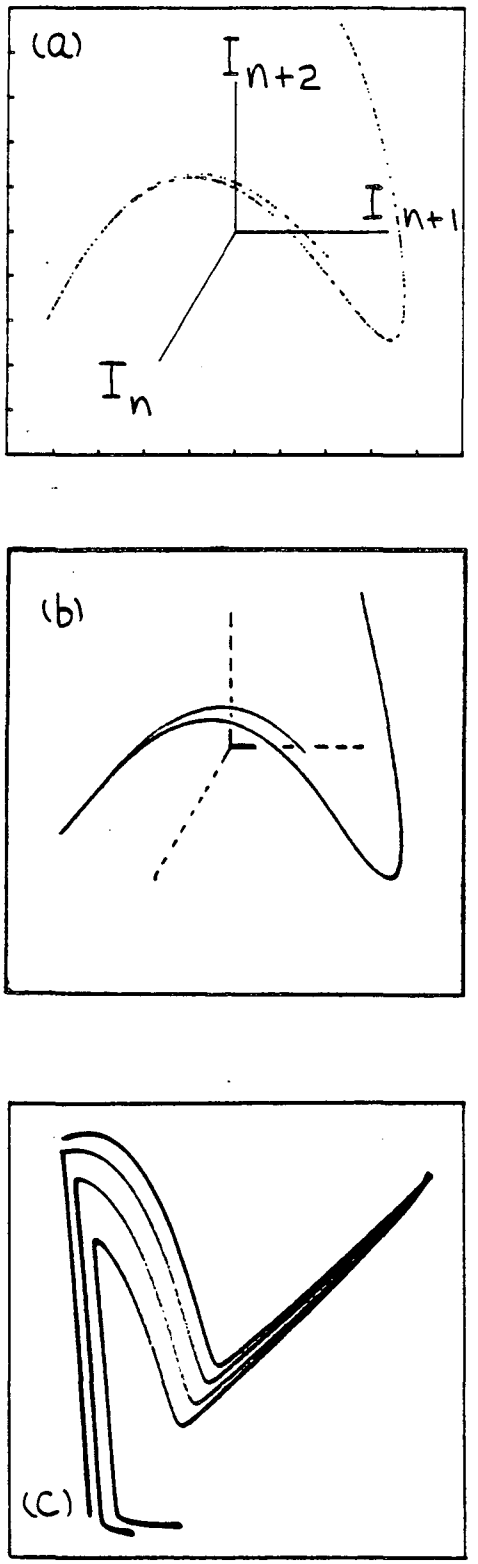

XBL 845-1946

Fig. 7

Top

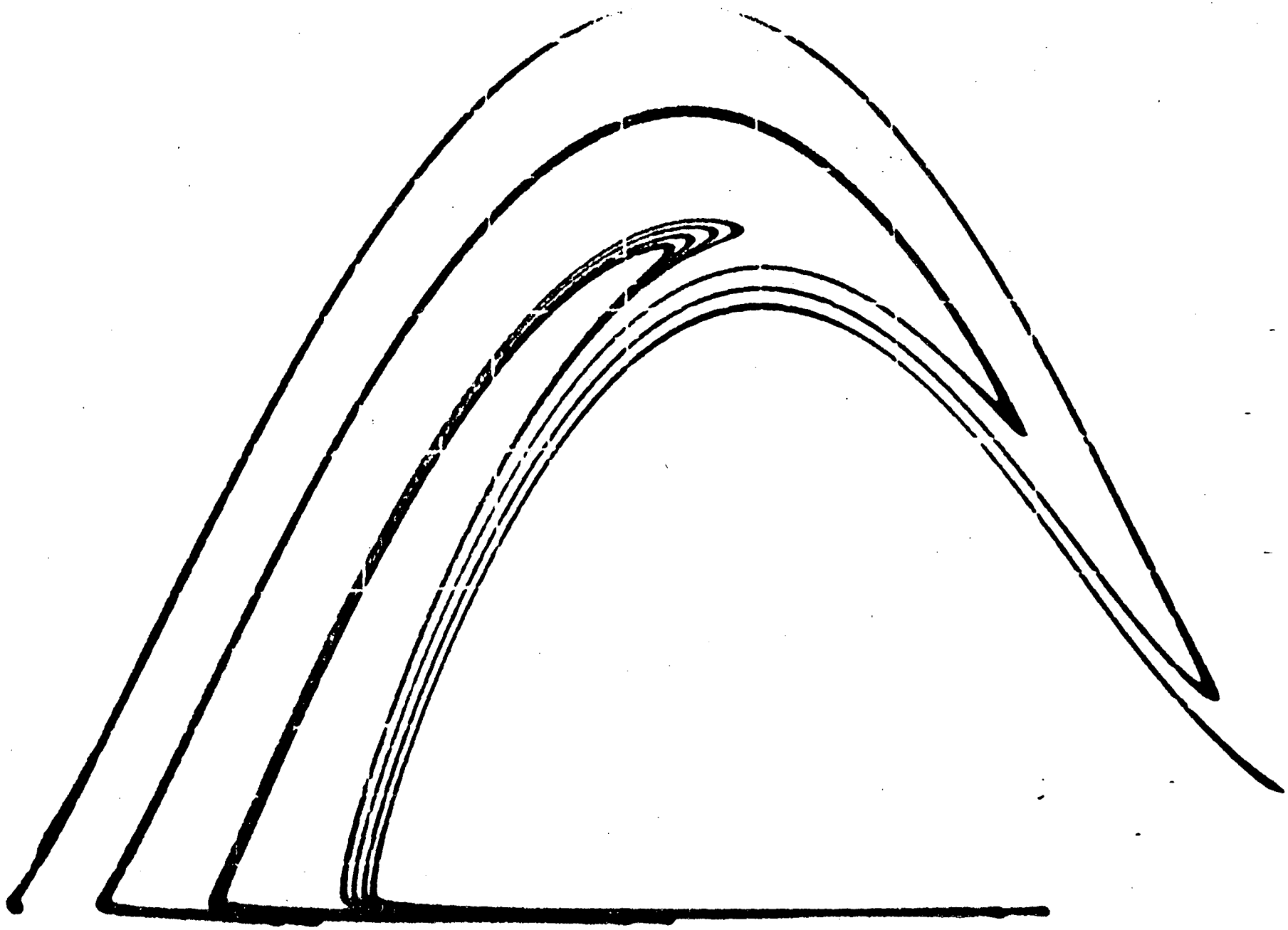

Fig. 8

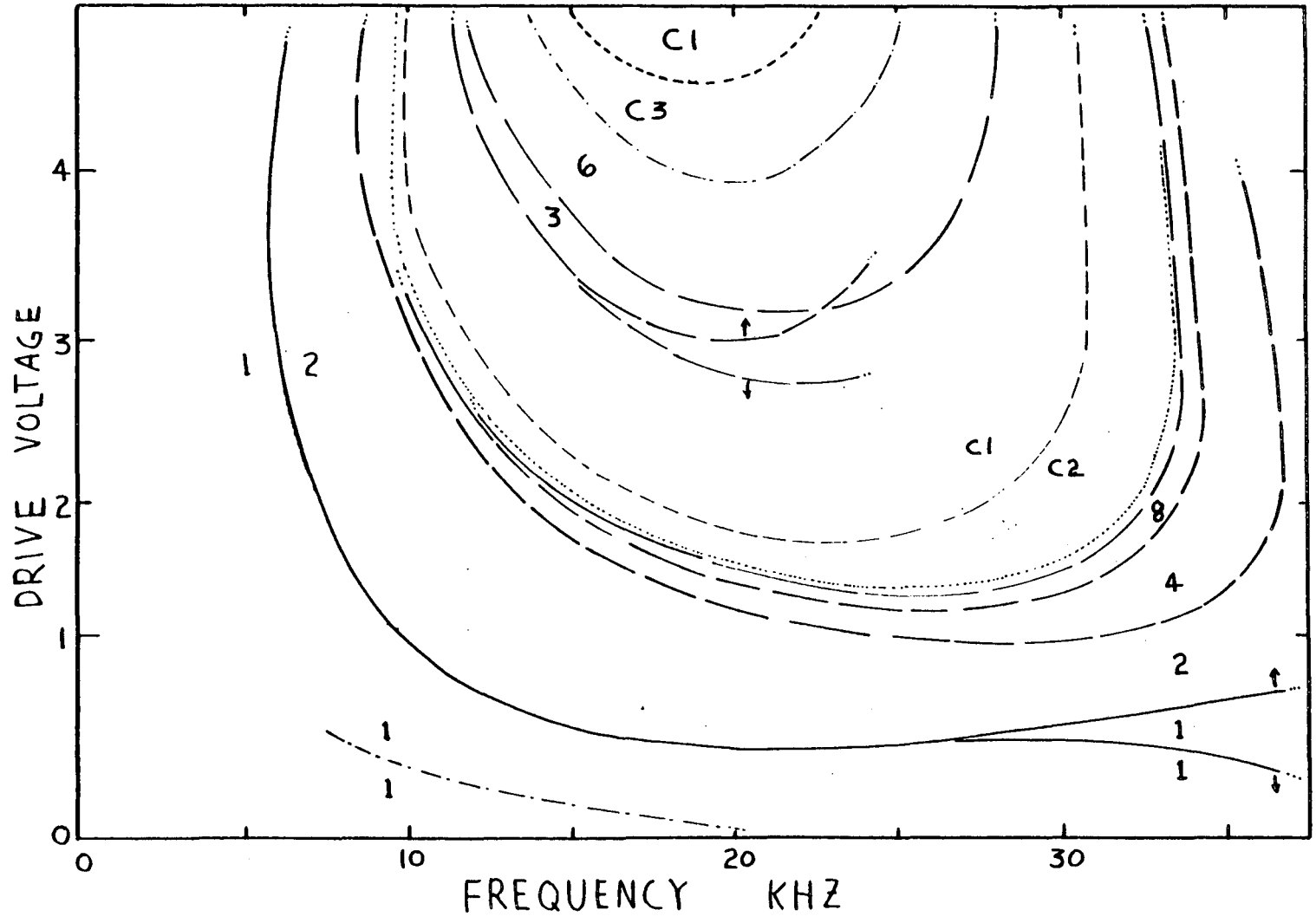

XBL 843-1221

Fig. 9

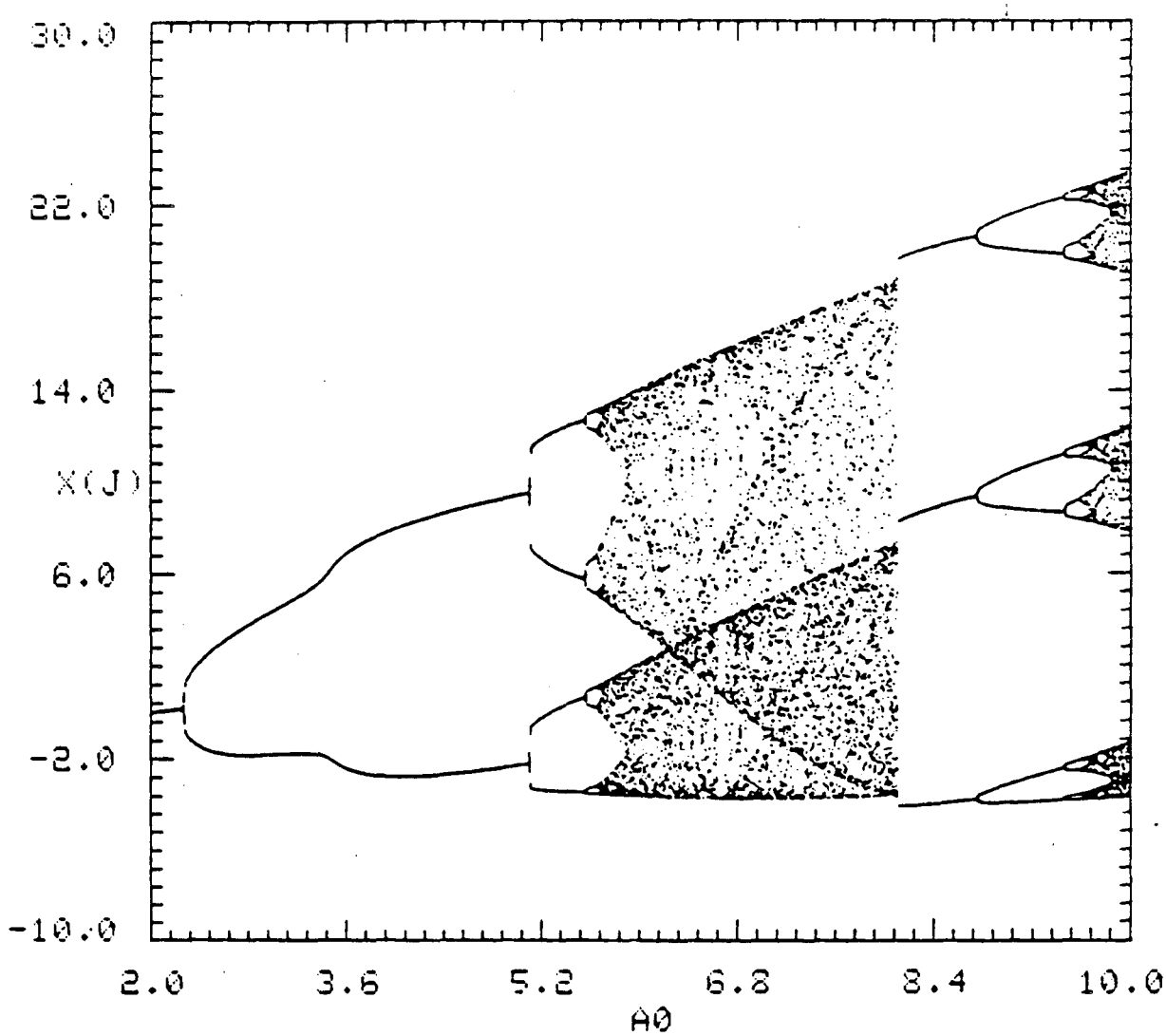

XBL 845-1873

Fig. 10

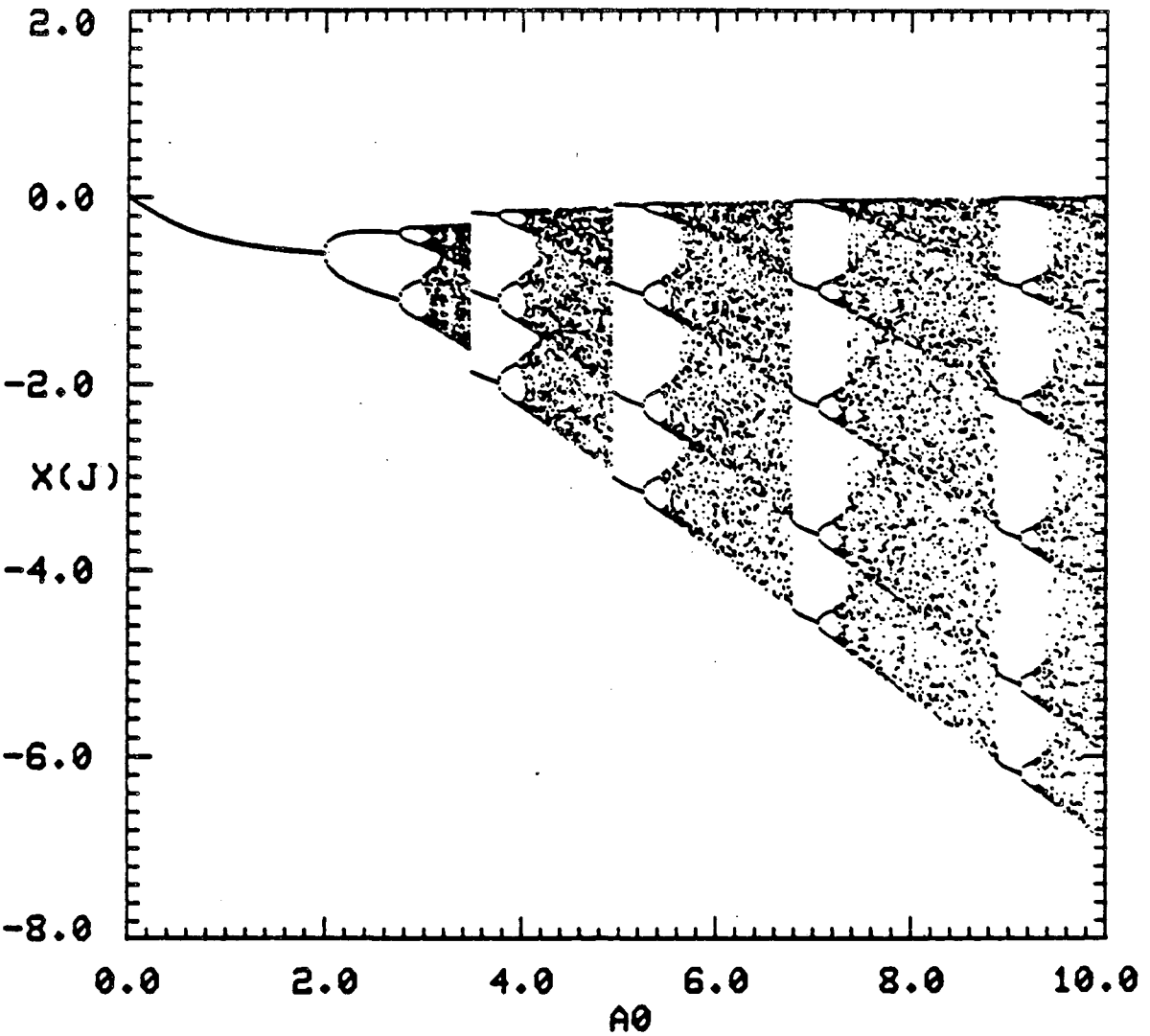

XBL 845-1874

Fig. 11

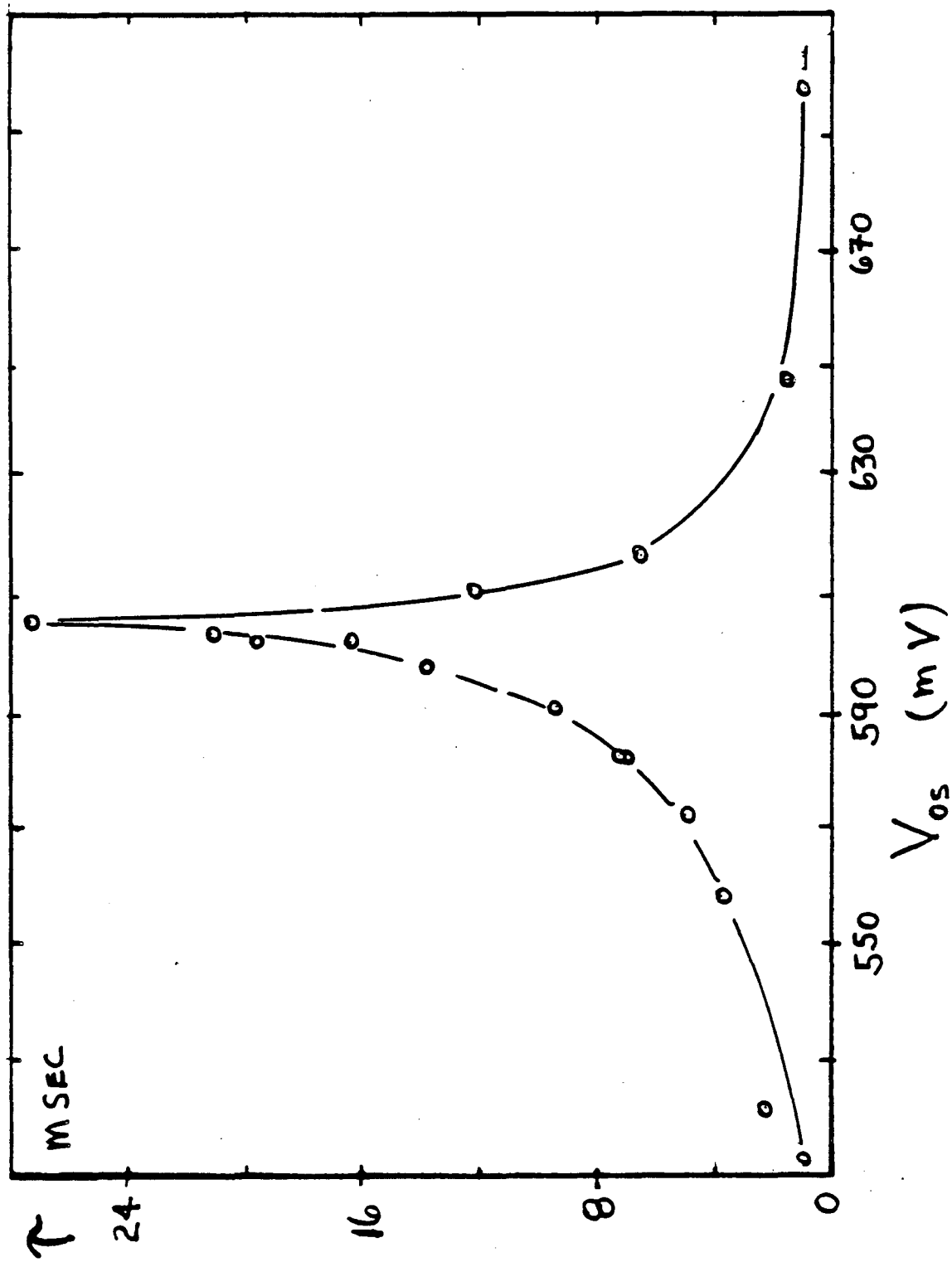

XBL 845-1951

Fig. 12

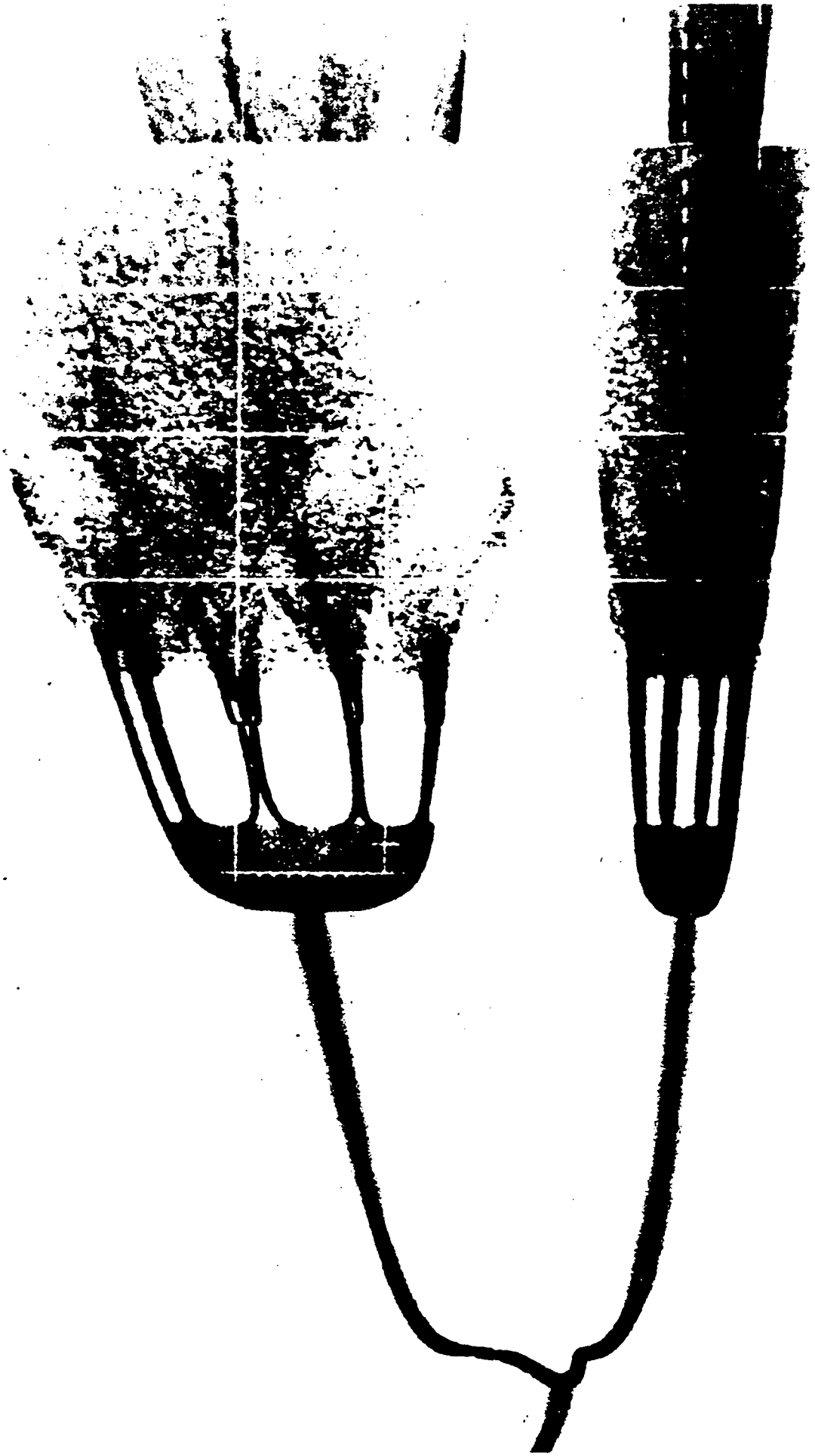

Fig. 13(a)

Top ↑

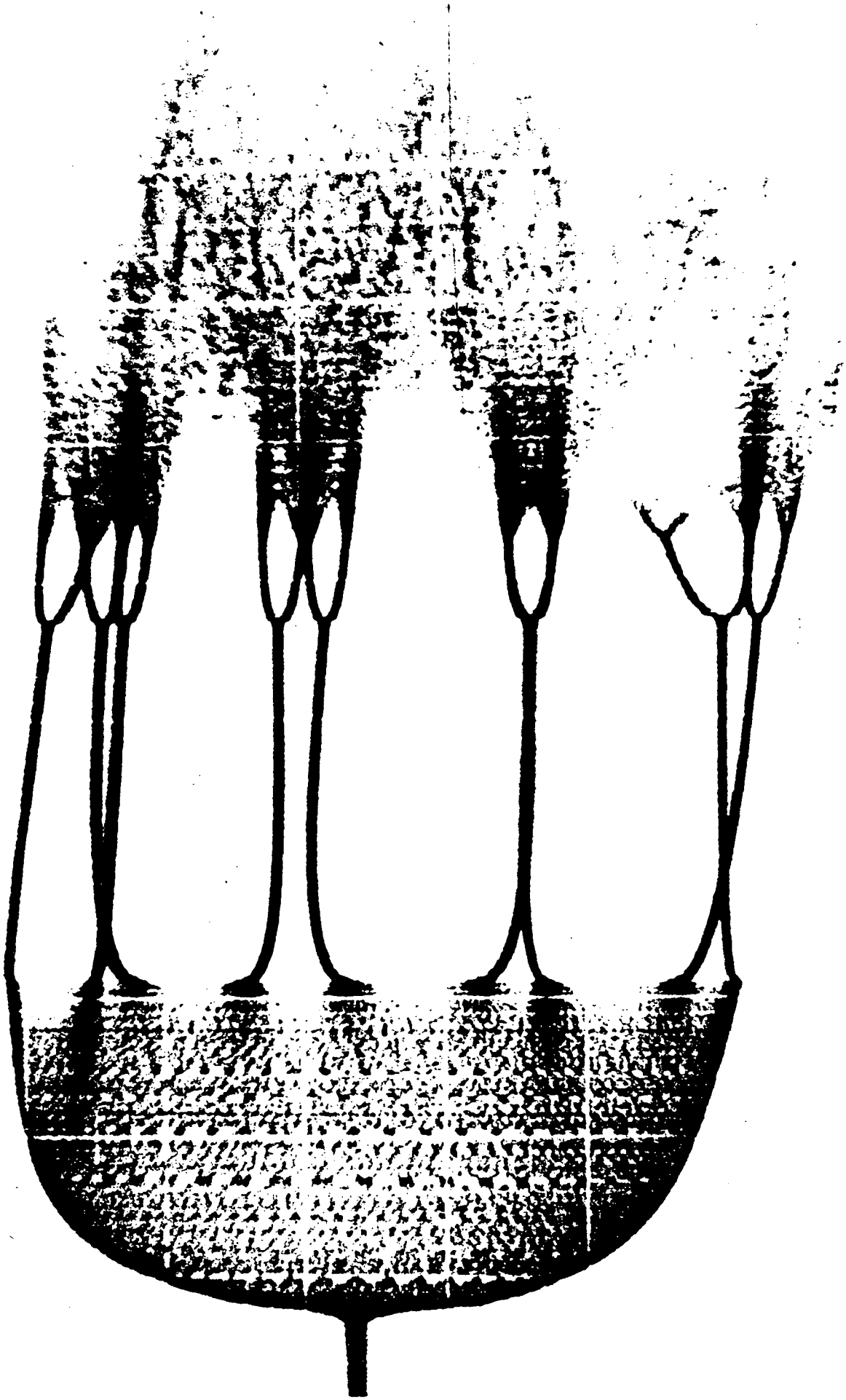

Fig. 13(b)

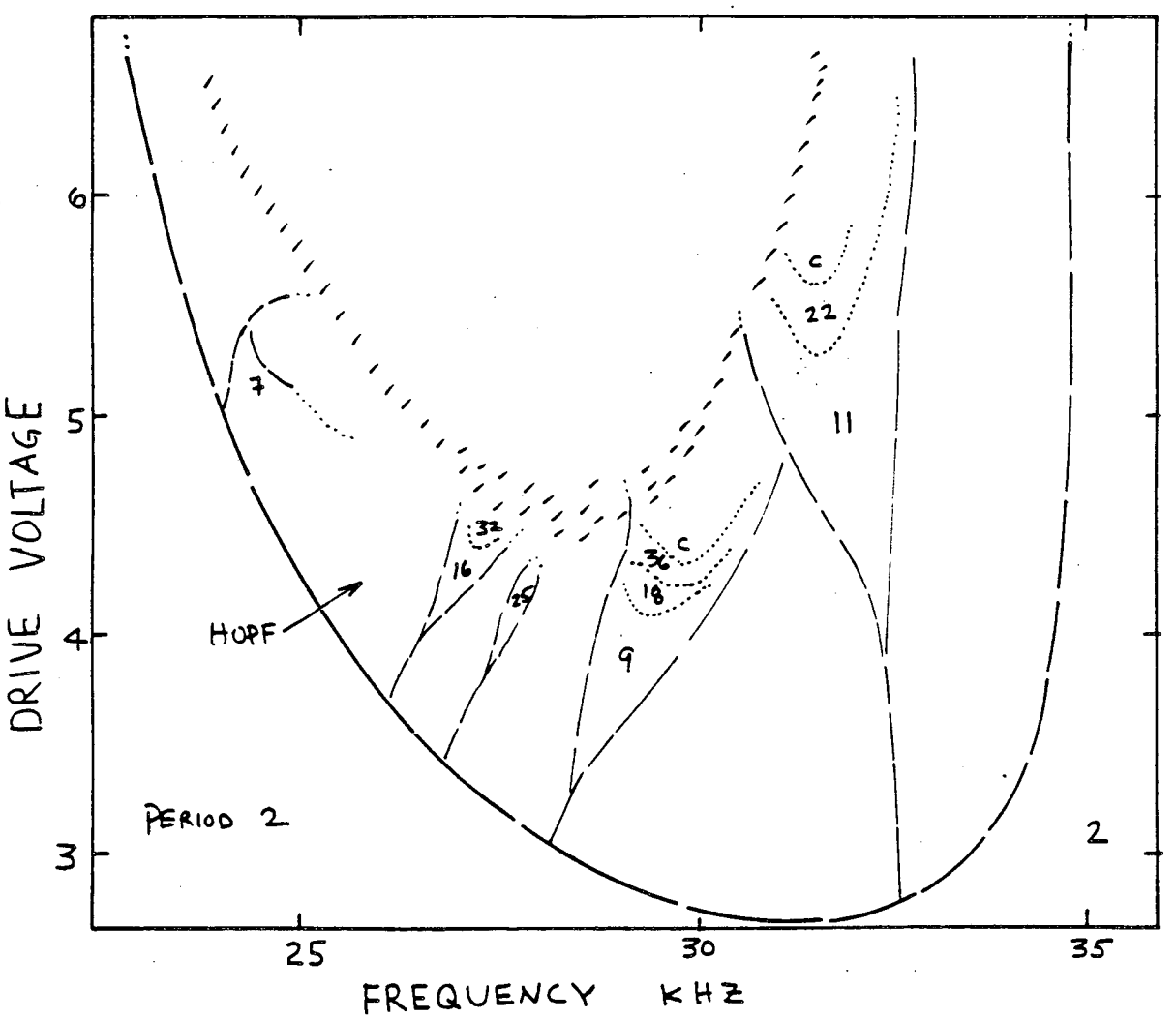

XBL 843-1220

Fig. 14

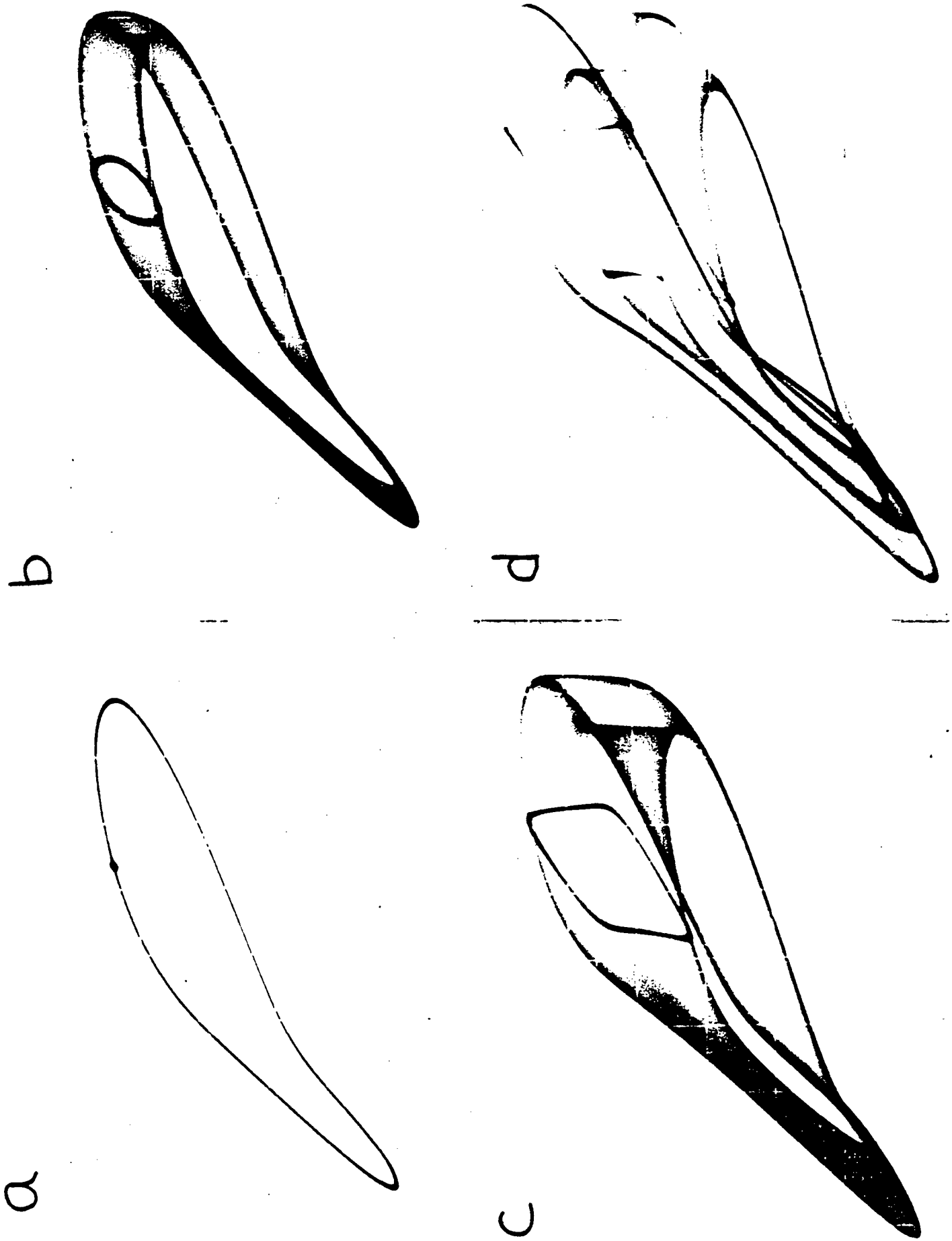

Fig. 15

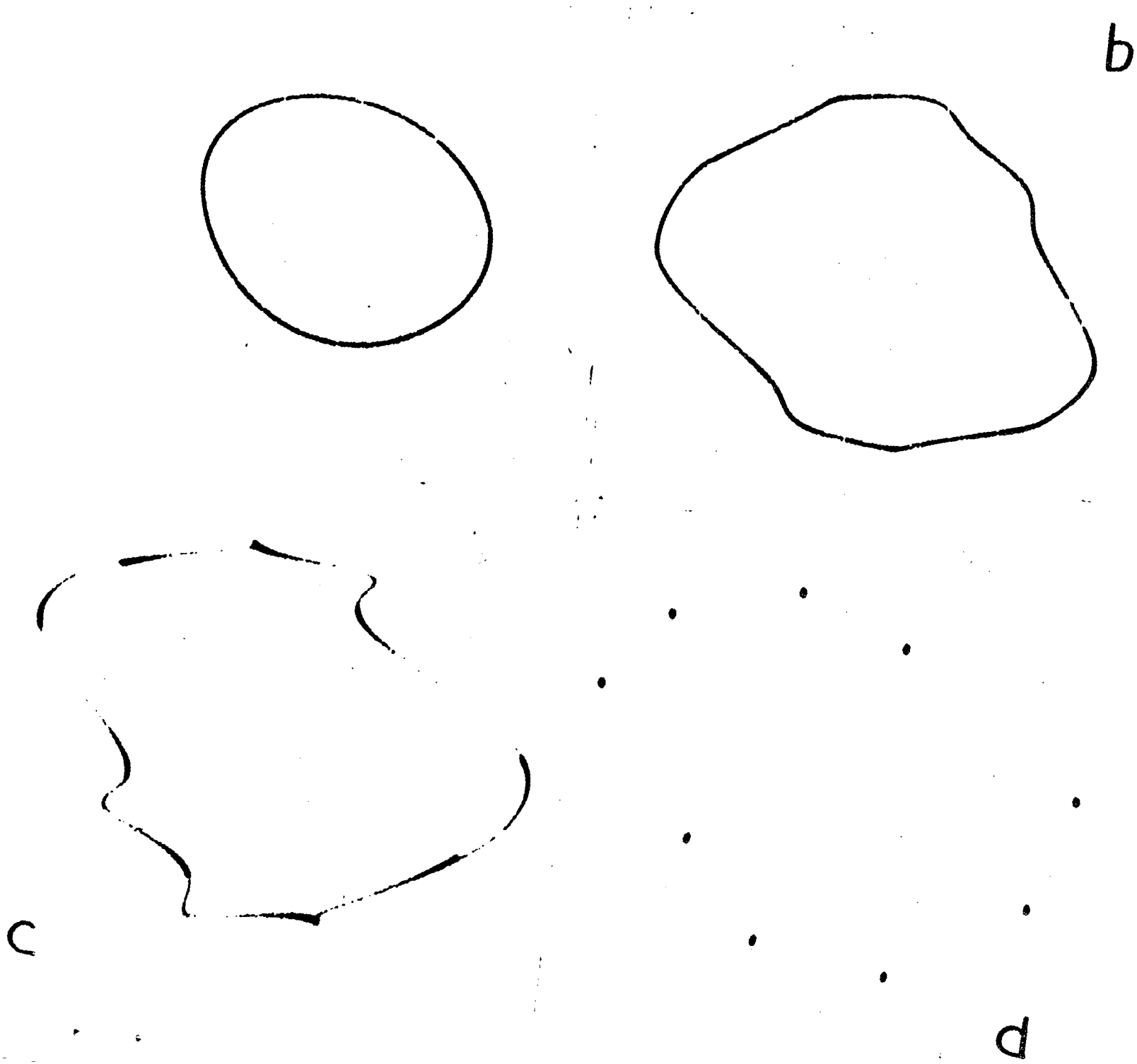

Fig. 1

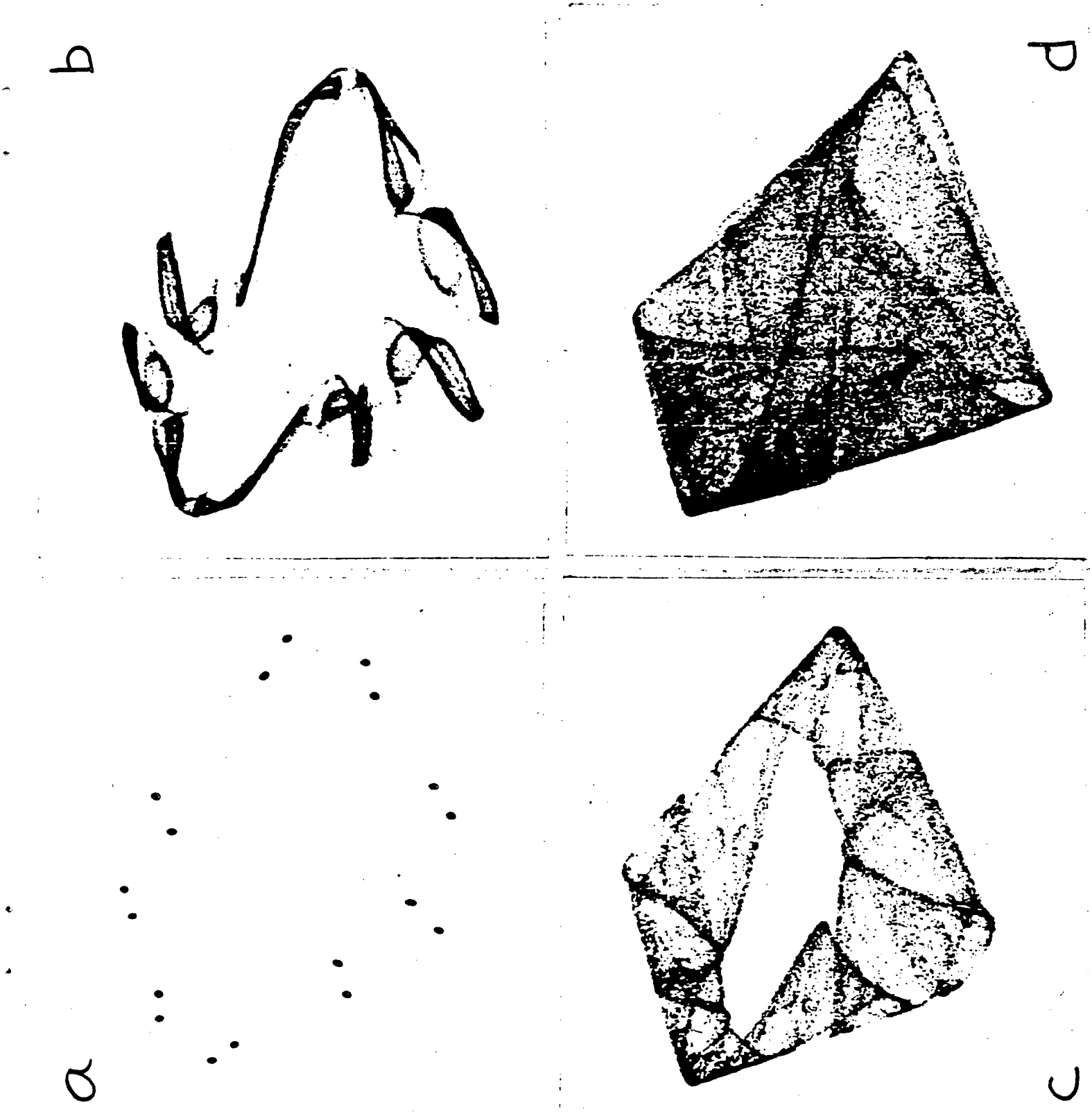

Fig. 17

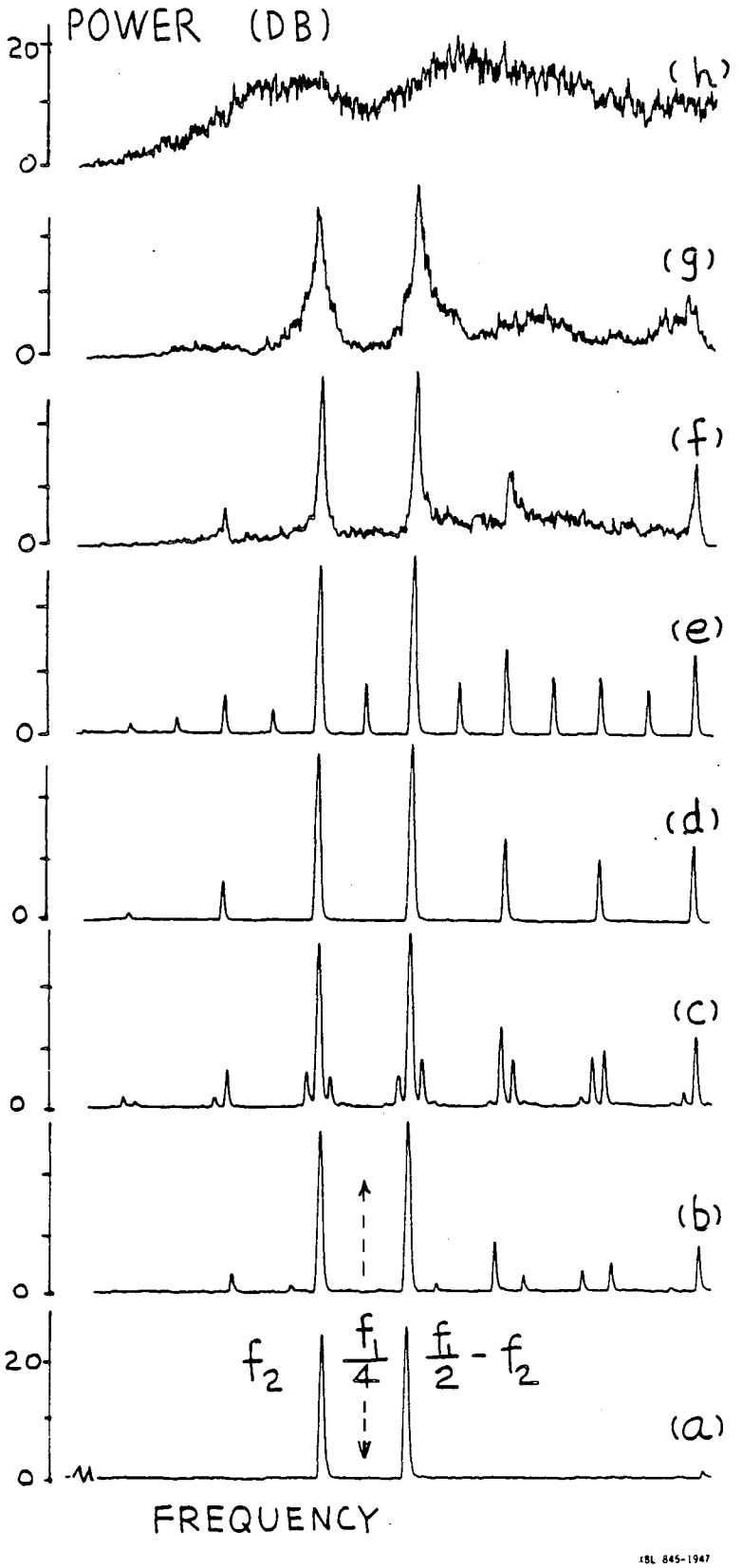
POWER (DB)
20
0
(h)
(g)
(f)
(e)
(d)
(c)
(b)
(a)
f_2
$\frac{f_1}{4}$
$\frac{f_1}{2} - f_2$
FREQUENCY
XBL 845-1947

Fig. 18

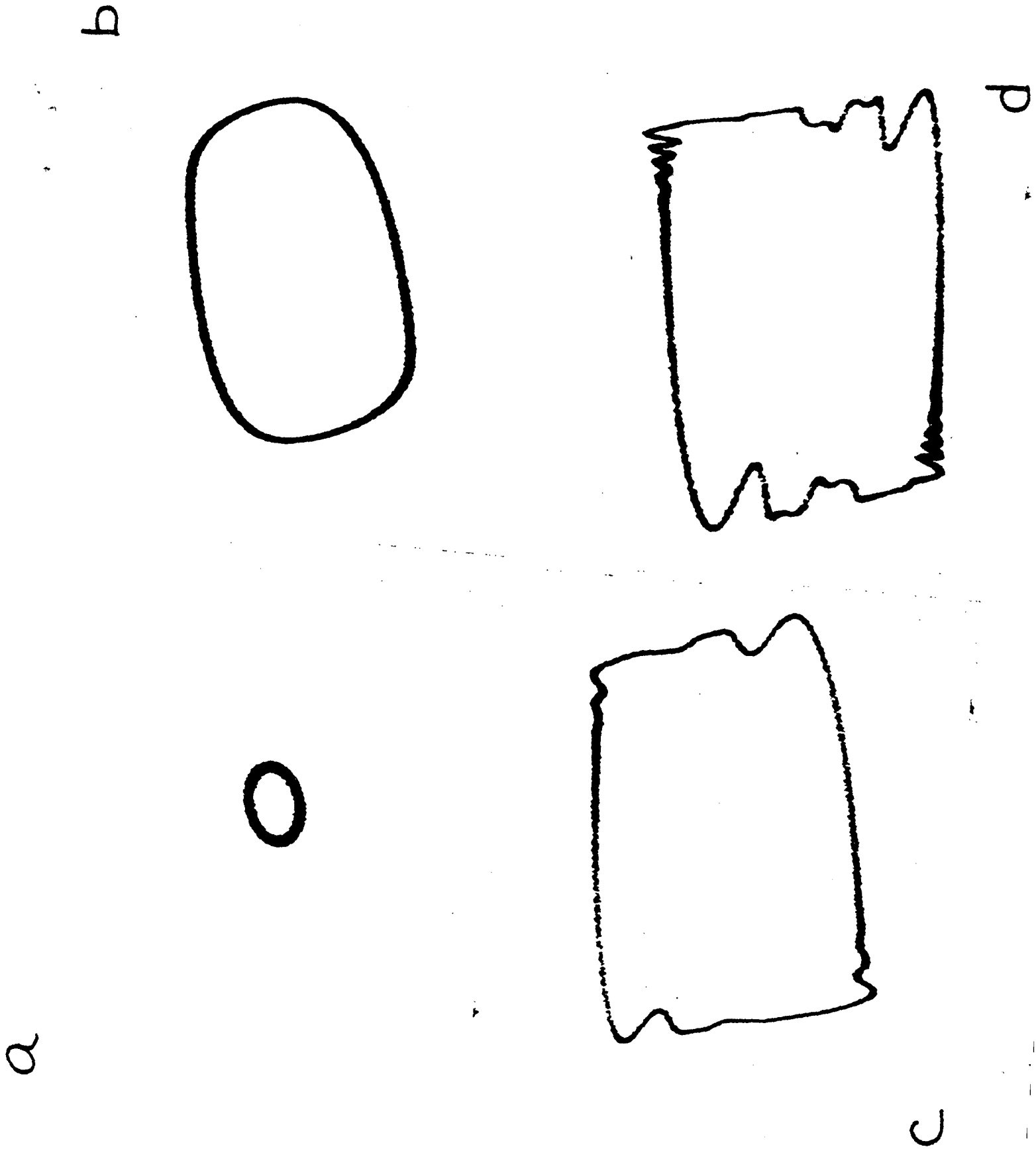

Fig. 19

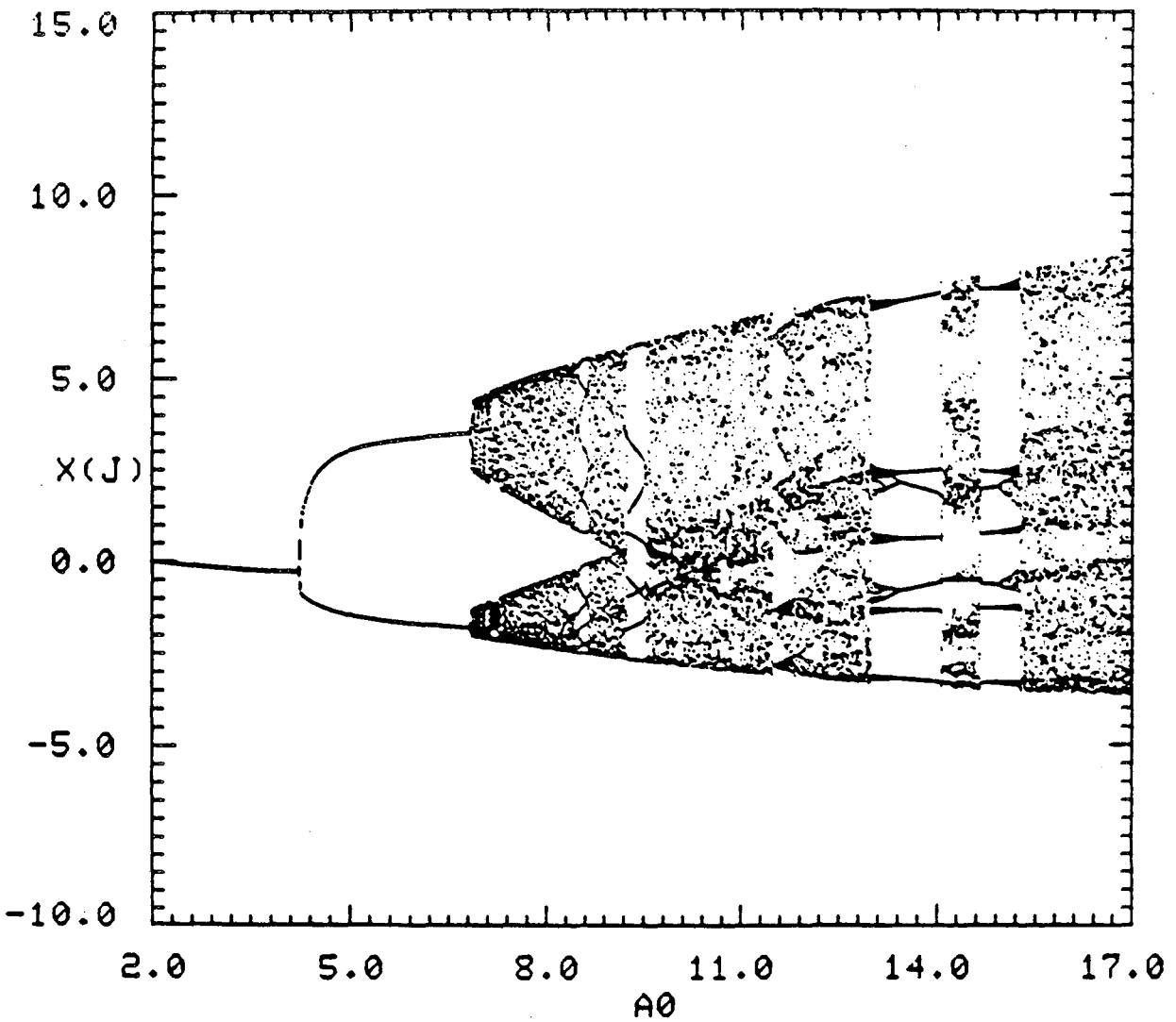

XBL 845-1971

Fig. 20

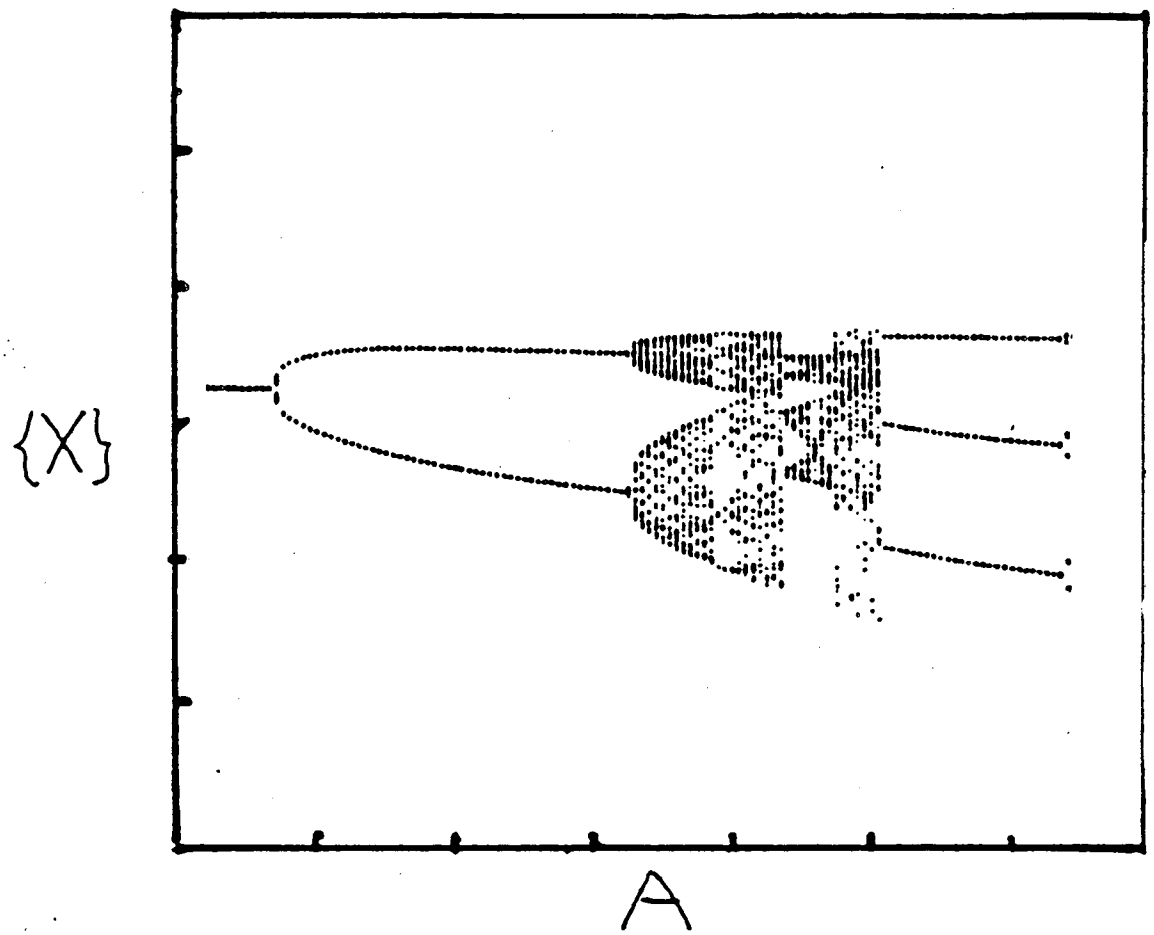

XBL 845-1972

Fig. 21

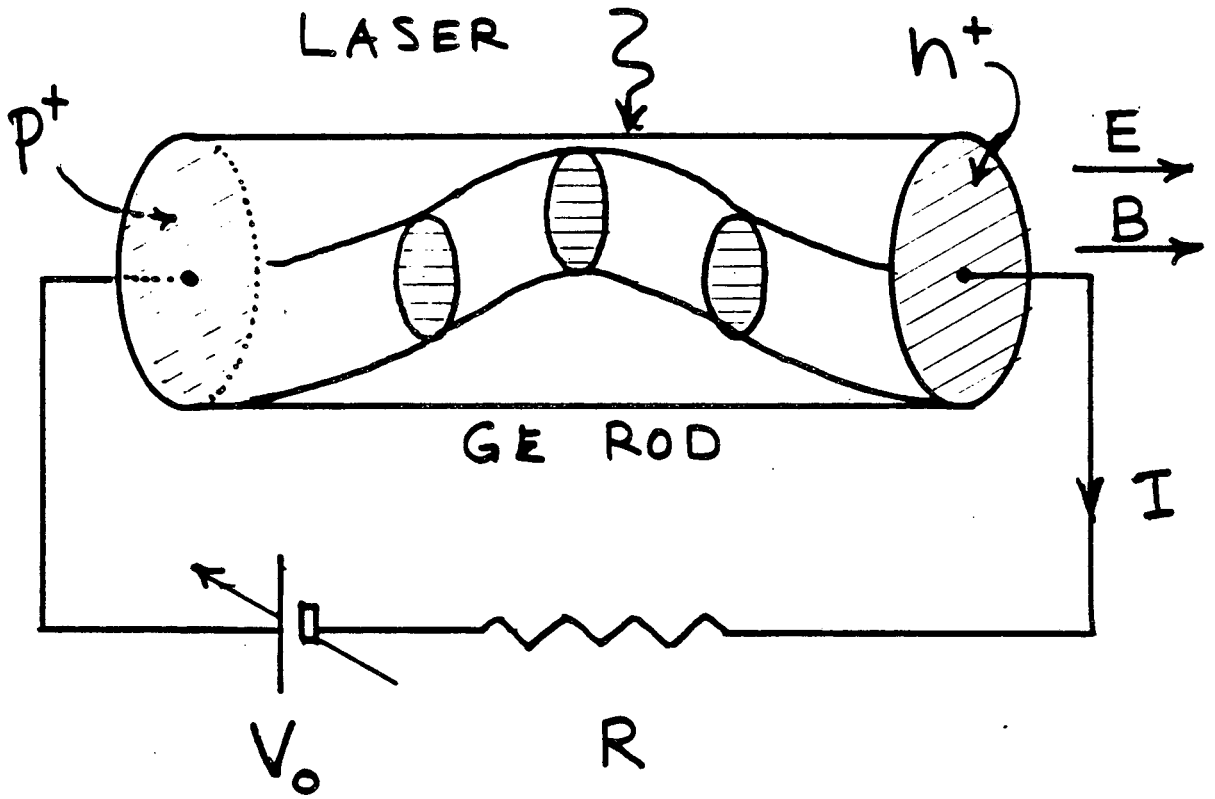

XBL 845-1953

Fig. 22

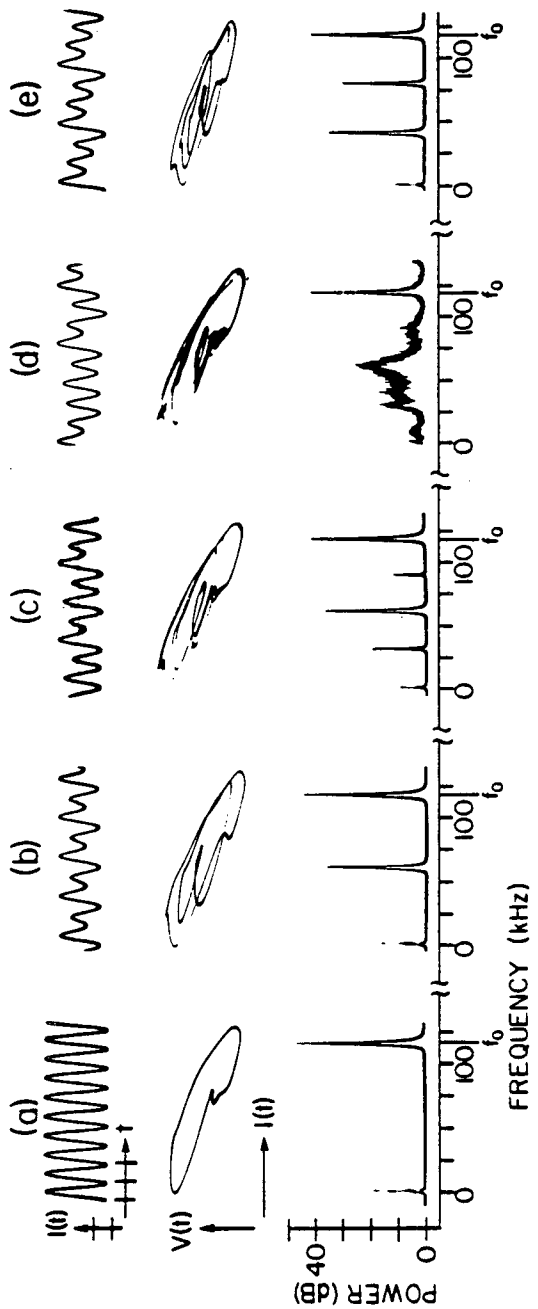

Fig. 23

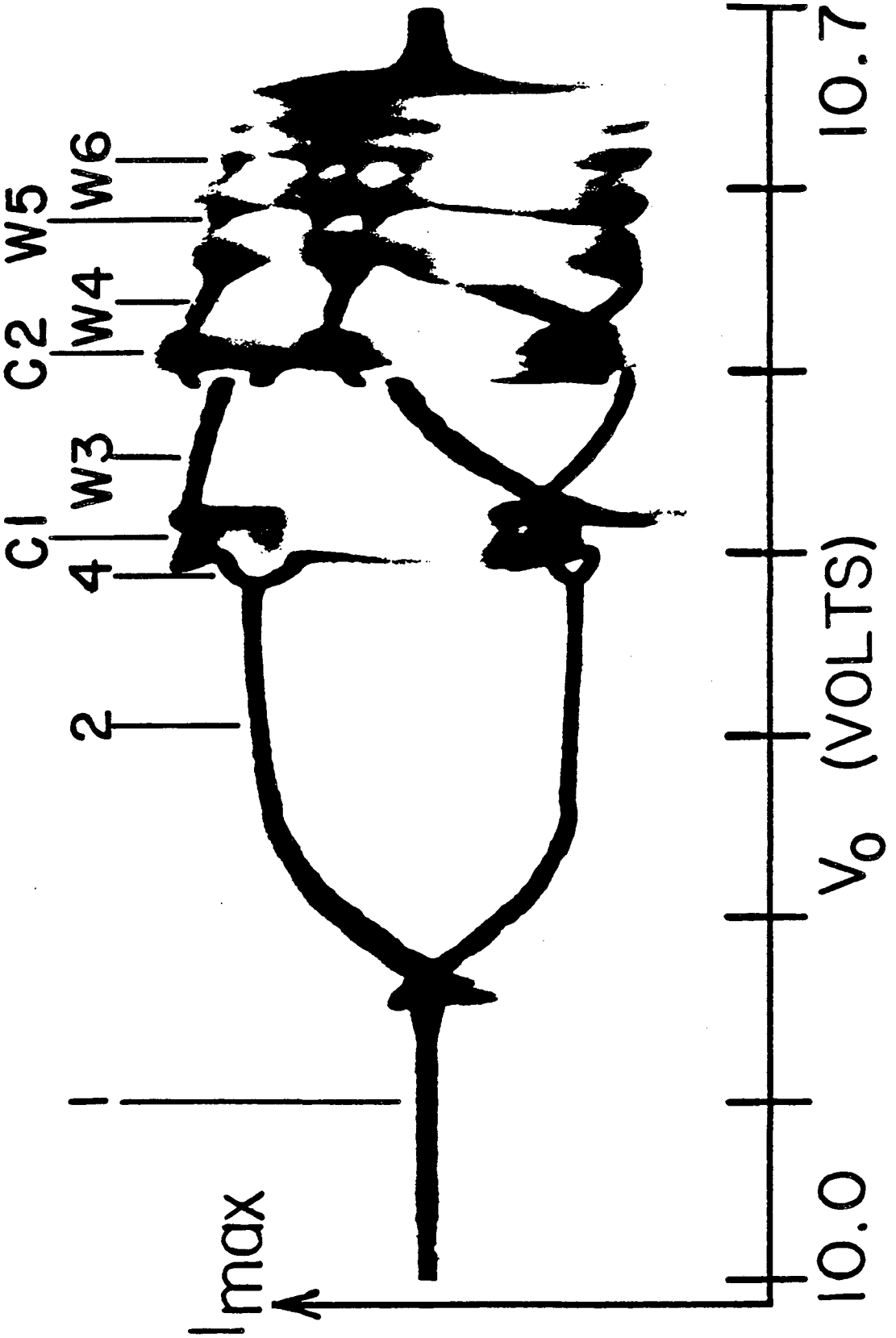

Fig. 24

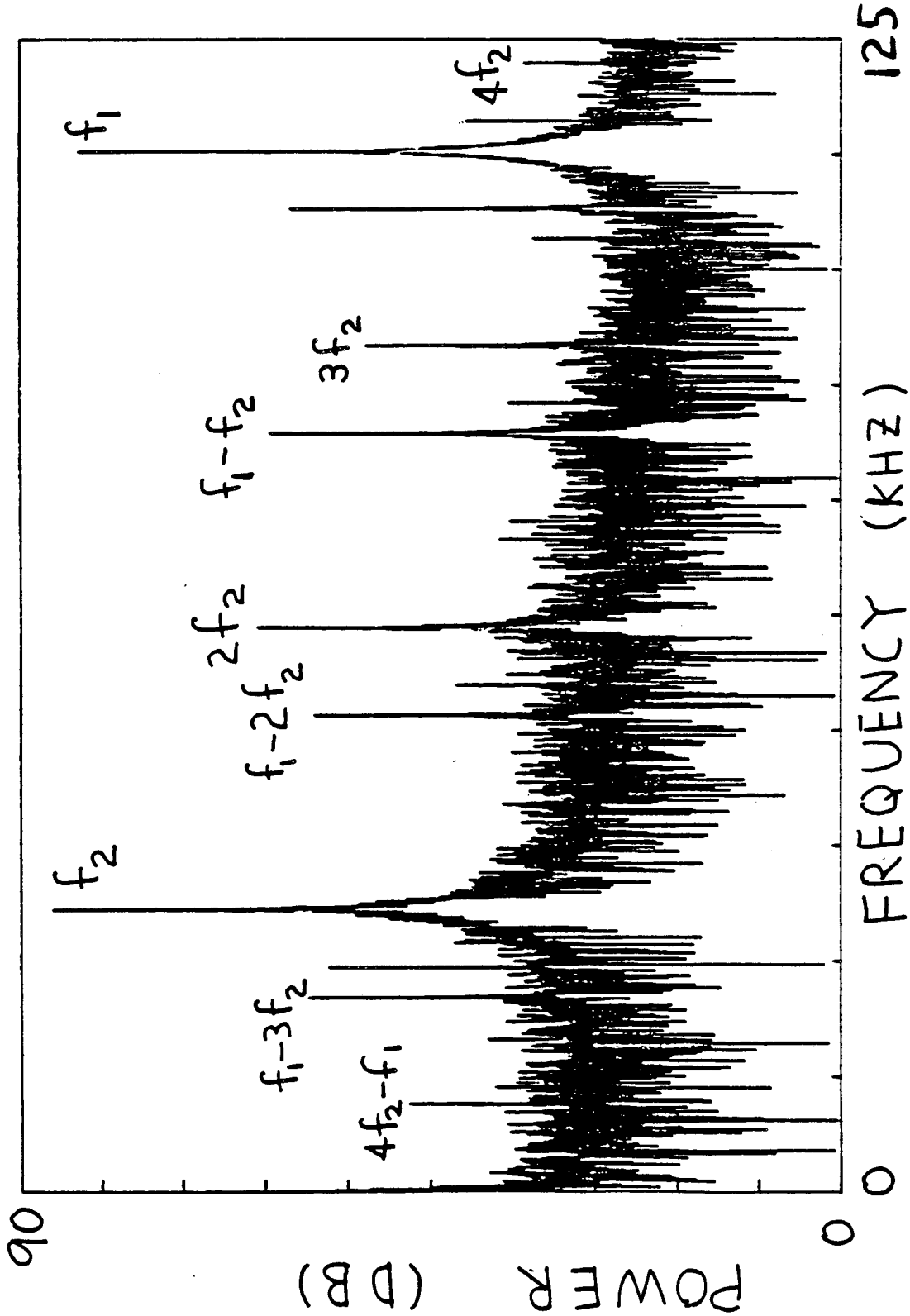

XBL 845-1949

Fig. 25

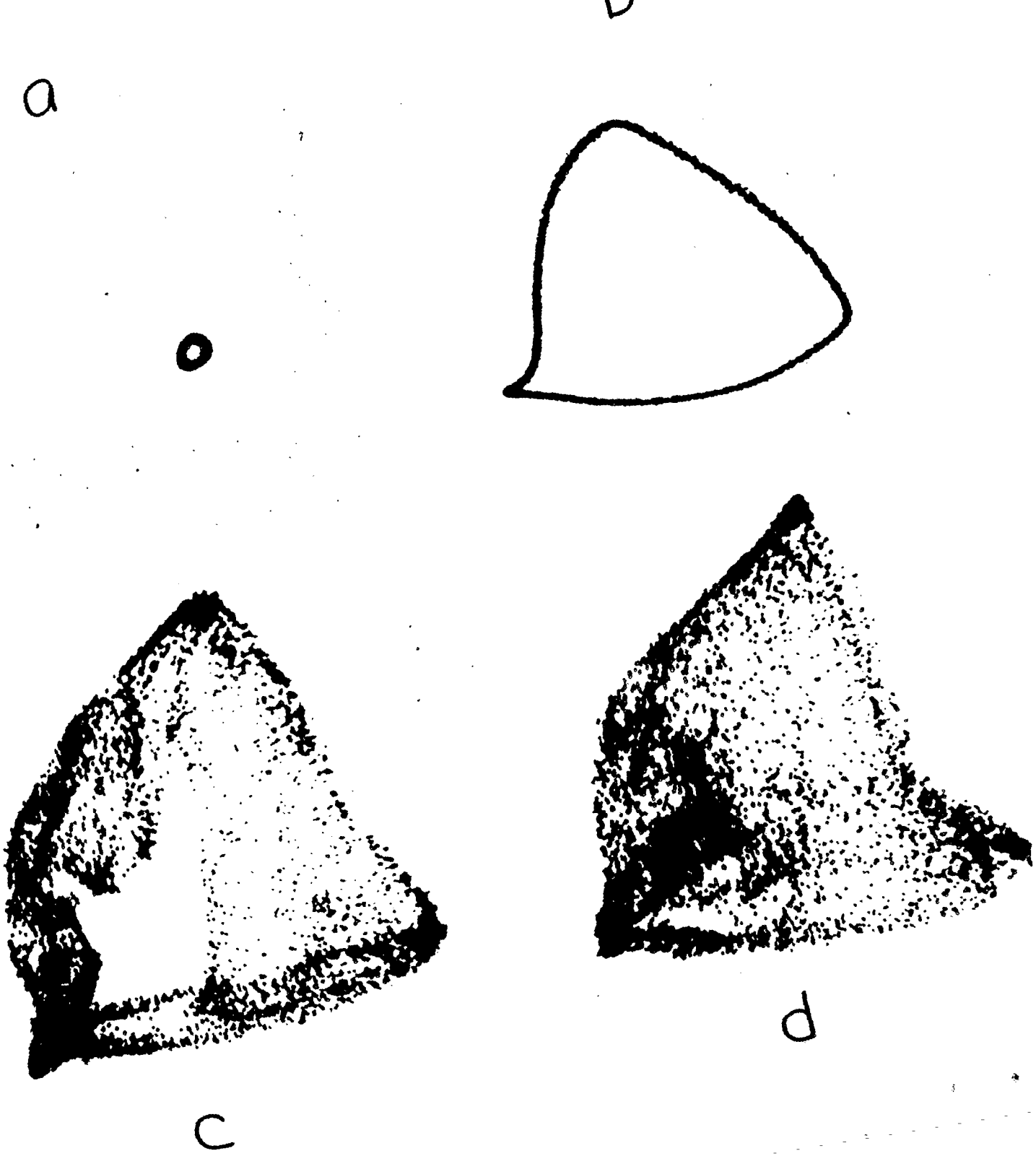

Fig.

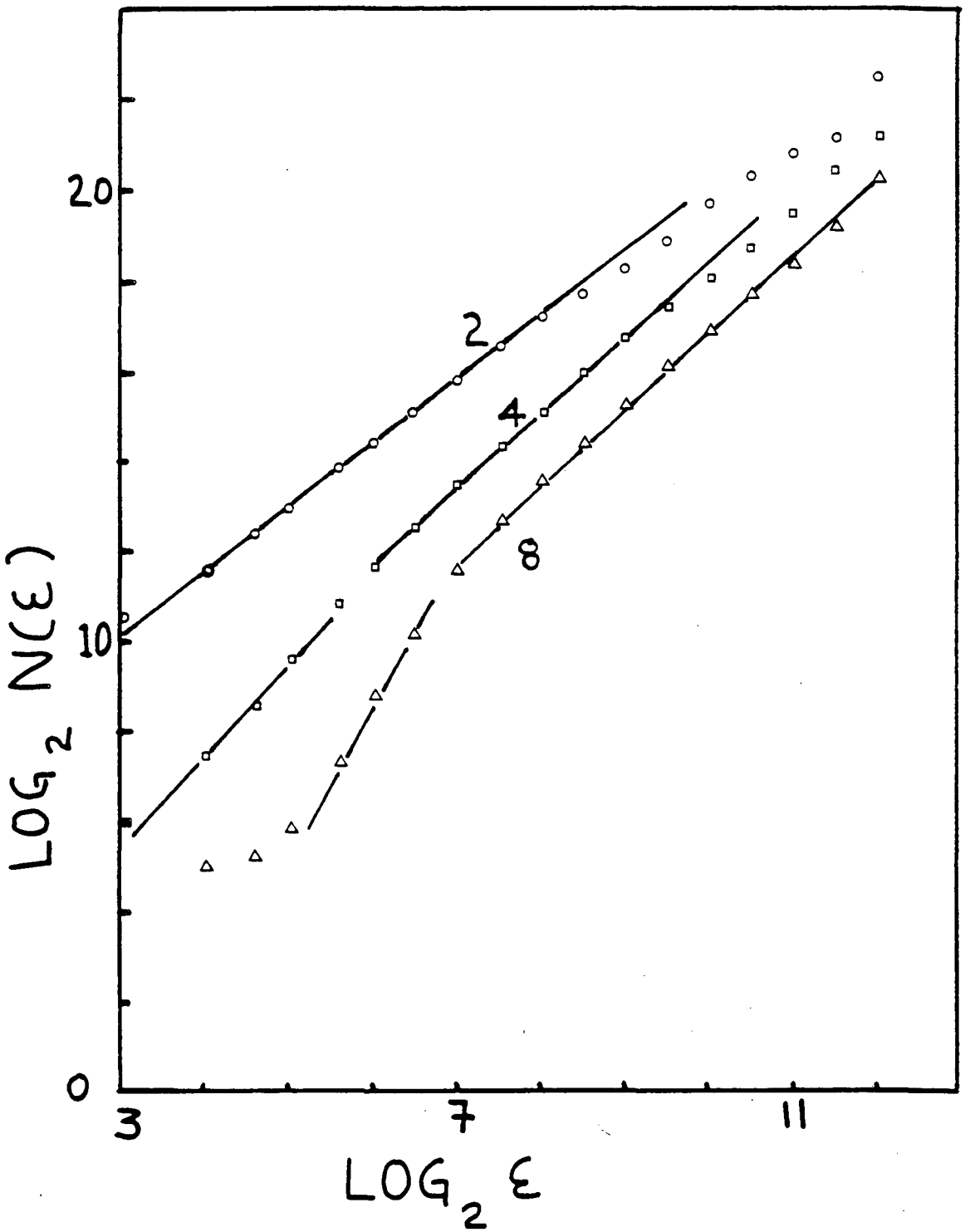

XBL 845-1952

Fig. 27

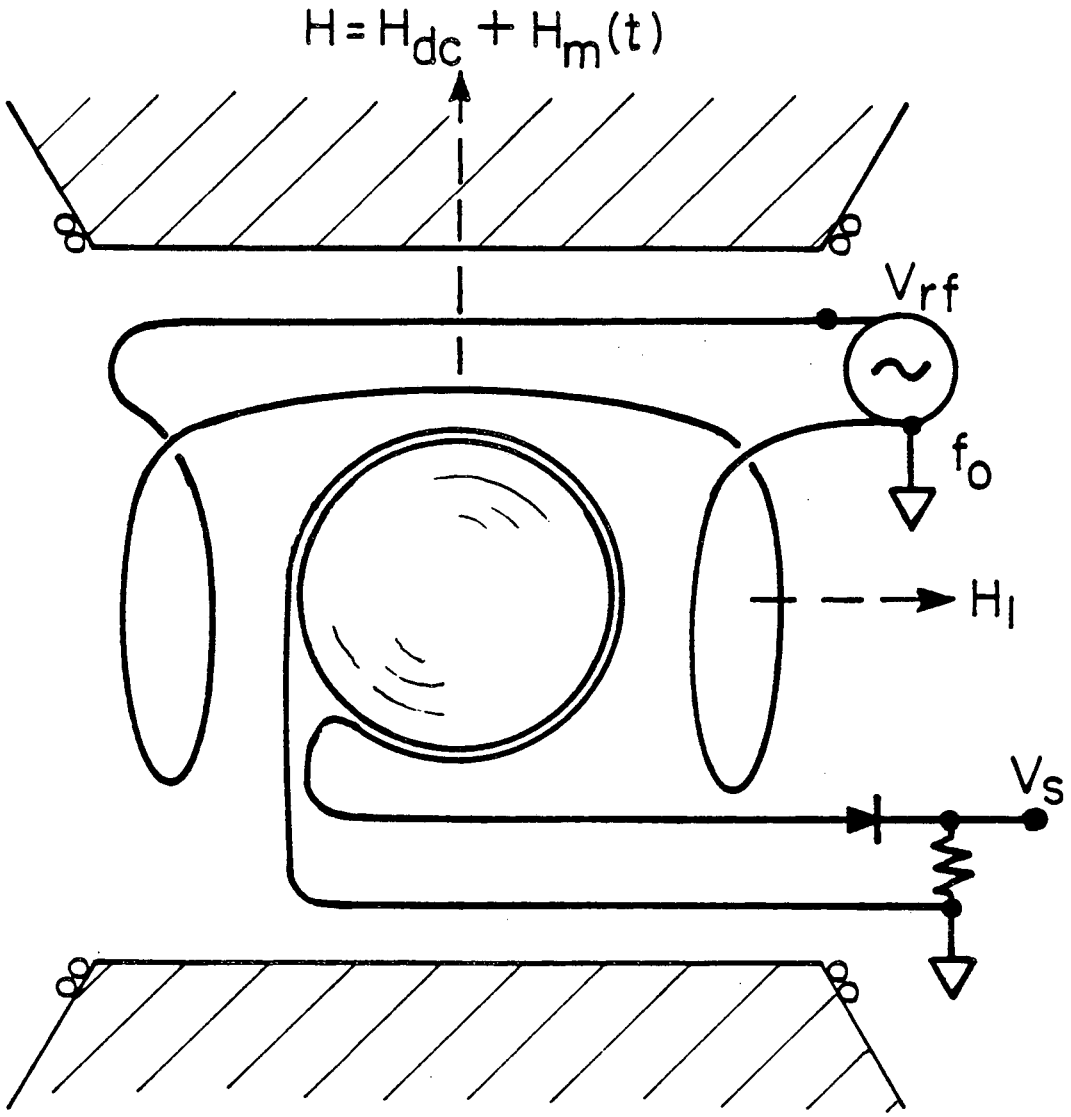

XBL8210-6686

Fig. 28

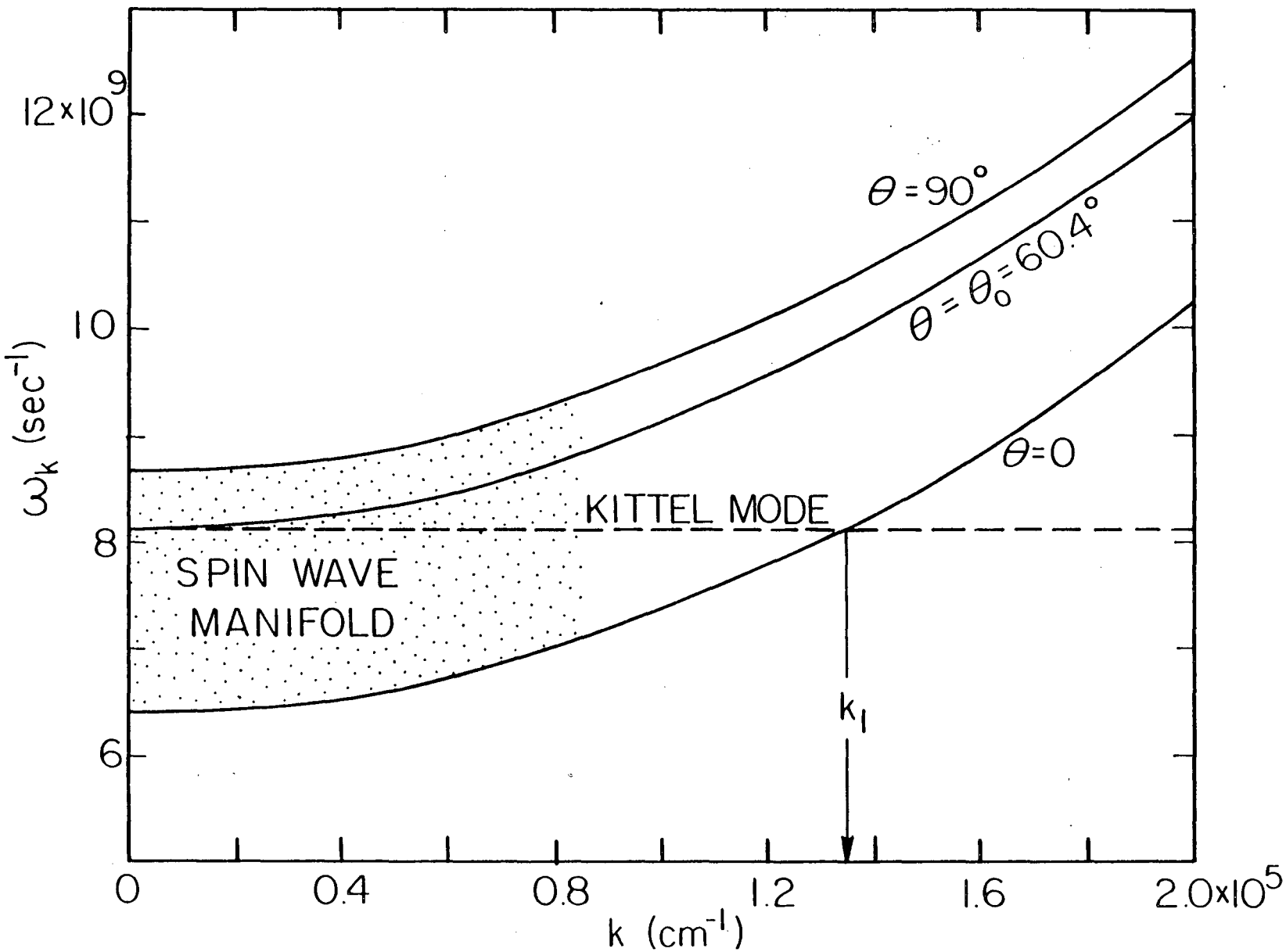

XBL839-6409

Fig. 29

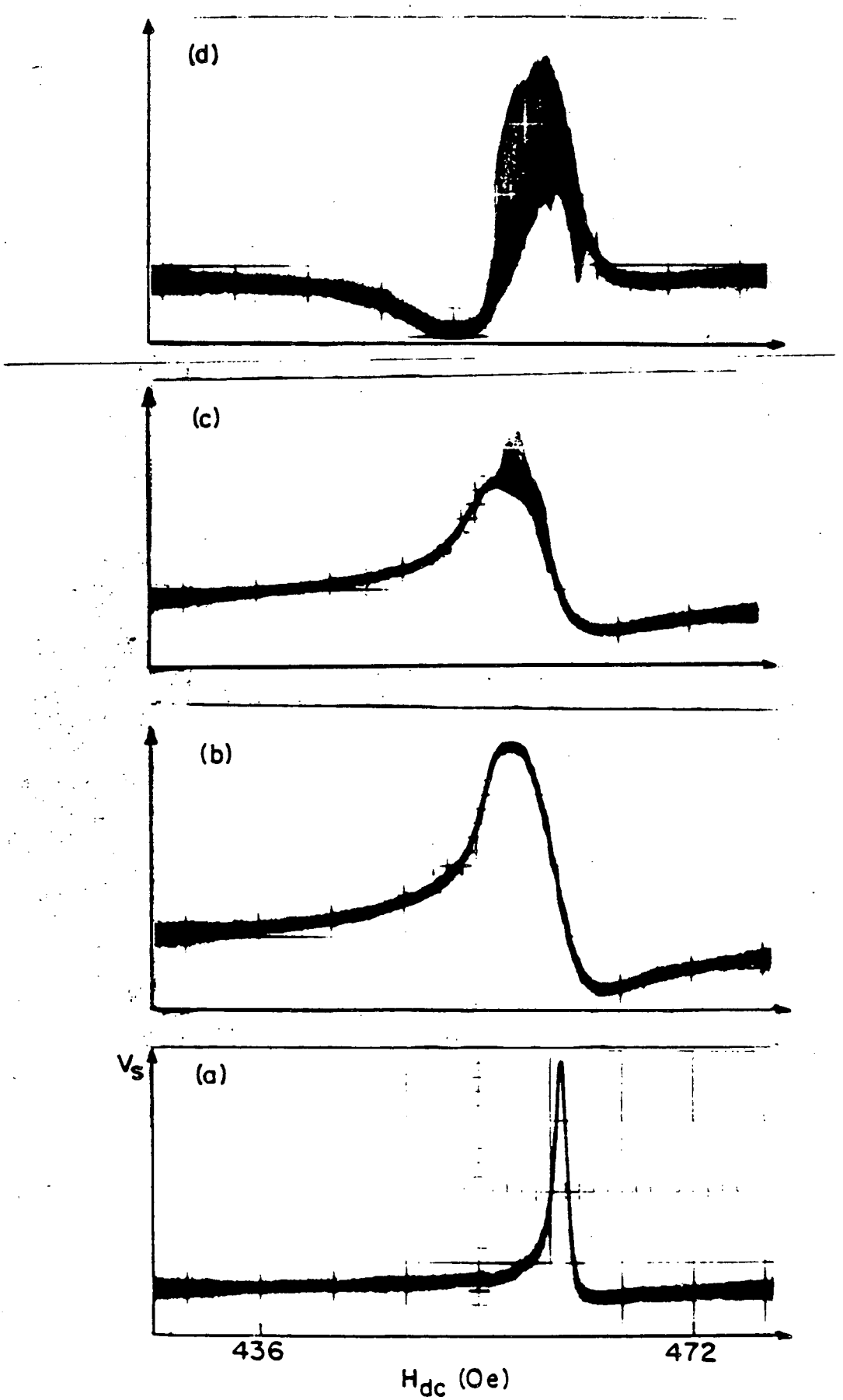

Fig. 30

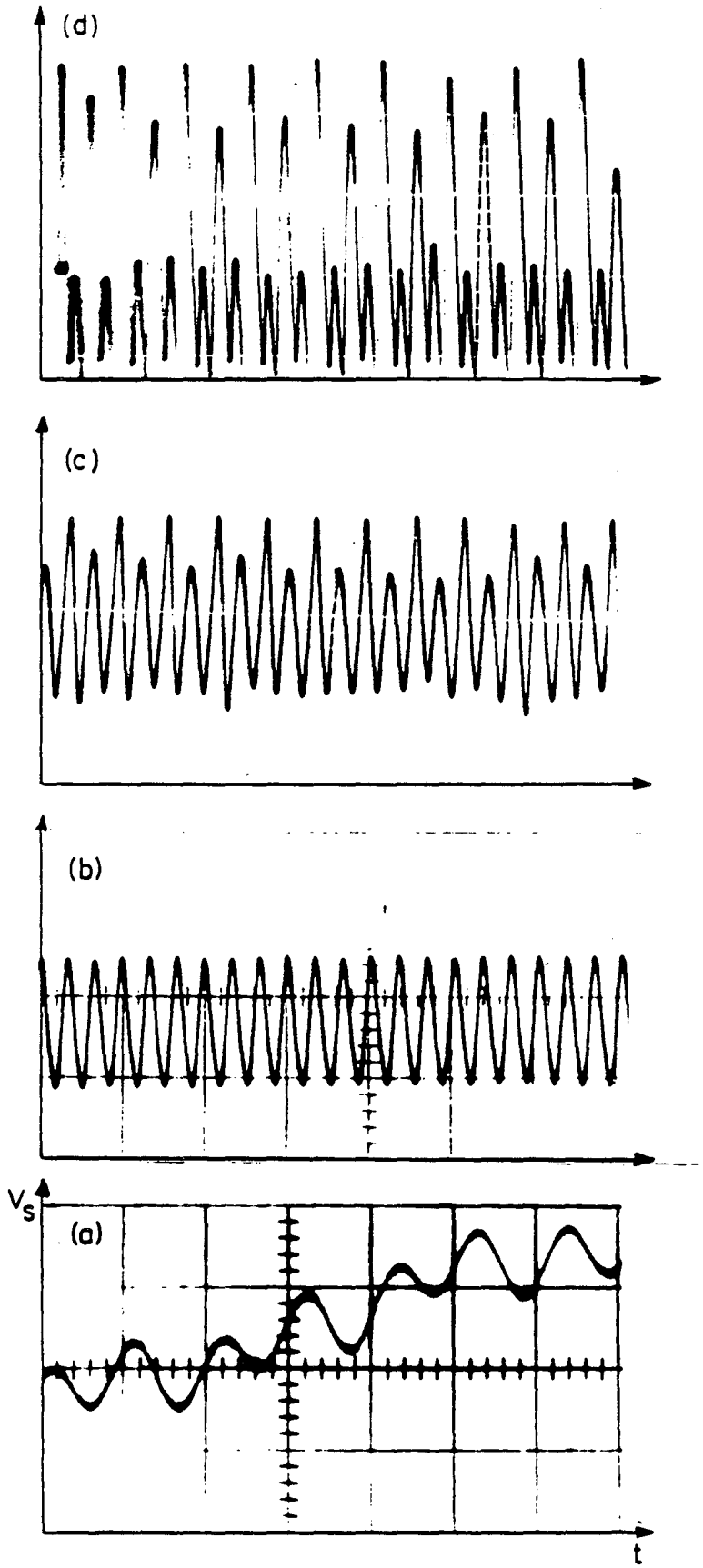

Fig. 31

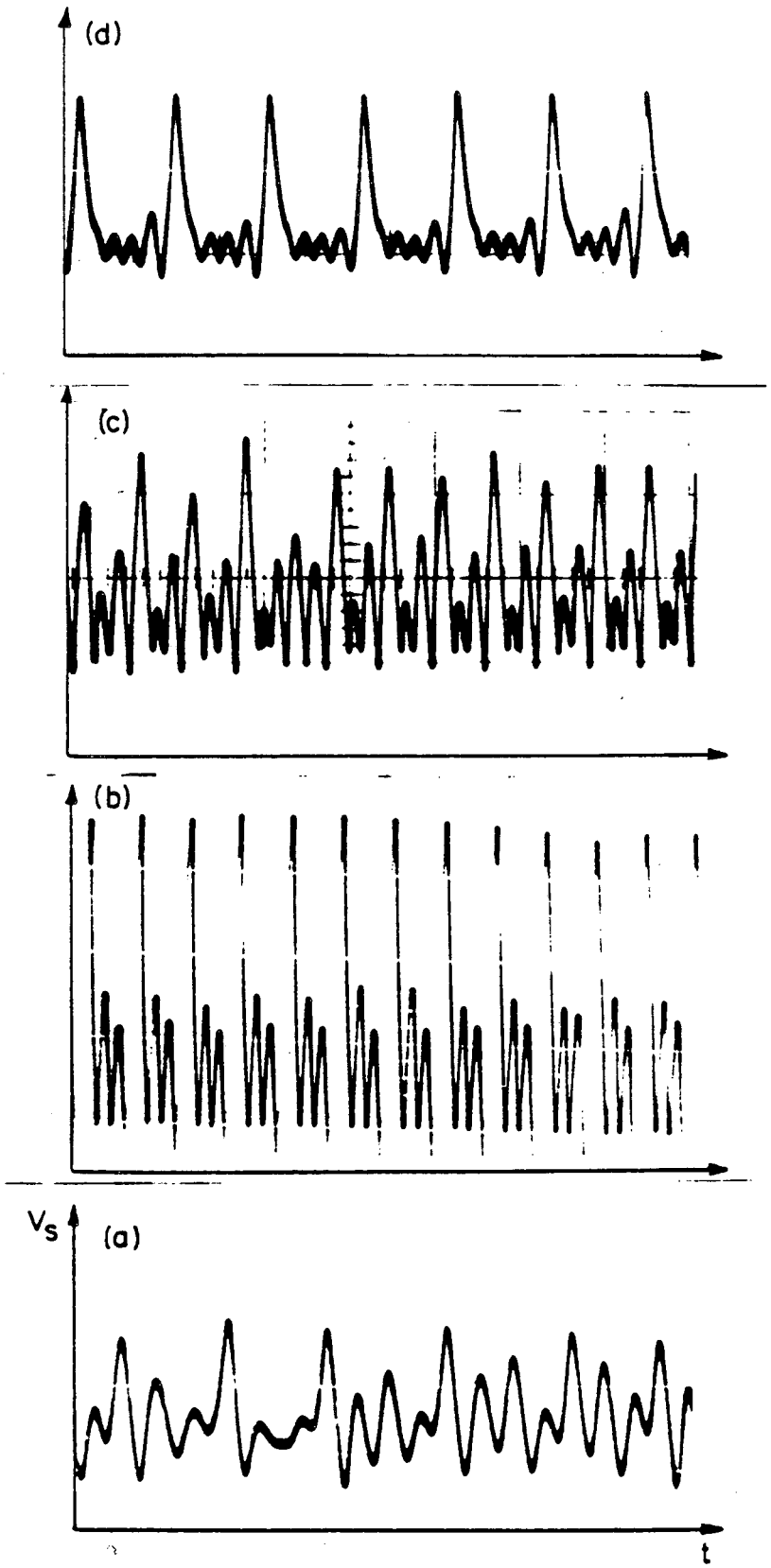

Fig. 32

This report was done with support from the Department of Energy. Any conclusions or opinions expressed in this report represent solely those of the author(s) and not necessarily those of The Regents of the University of California, the Lawrence Berkeley Laboratory or the Department of Energy.

Reference to a company or product name does not imply approval or recommendation of the product by the University of California or the U.S. Department of Energy to the exclusion of others that may be suitable.

TECHNICAL INFORMATION DEPARTMENT
LAWRENCE BERKELEY LABORATORY
UNIVERSITY OF CALIFORNIA
BERKELEY, CALIFORNIA 94720